Journal of Materials Chemistry A

ROYAL SOCIETY OF CHEMISTRY

PAPER

View Article Online
View Journal | View Issue

Cite this: *J. Mater. Chem. A*, 2024, **12**, 15163

Implication of surface oxidation of nanoscale molybdenum carbide on electrocatalytic activity†

Siying Yu, Ankit Kumar Gautam, Di Gao, Andrew N. Kuhn, Haozhen He, Alexander V. Mironenko * and Hong Yang *

Transition metal carbides, such as molybdenum carbides, are promising substitutes for noble metals as low-cost, durable electrocatalysts. Under ambient conditions, however, these carbides are subject to oxidation due to their oxophilic nature. The partially oxidized surface may possess both oxygen-modulated metallic-like hydrogen adsorption sites and Brønsted-acidic hydroxyl sites. However, the impact of surface oxidation on electrochemical processes such as the hydrogen evolution reaction (HER) has rarely been studied. Here, we synthesized β-Mo_2C catalysts and oxidized their surfaces electrochemically to varying extents to study the effects of surface oxidation on HER activity. The degree of surface oxidation was controlled by applying different potential windows to metal carbide catalysts. The samples with varying degrees of surface oxidation were tested for their HER activity. Experimental data indicate that the Tafel slope for the HER and double-layer capacitance were negatively affected by surface oxidation, particularly due to the loss of carbon and the formation of electrochemically less active surface oxides. The surface oxidation was studied experimentally by X-ray photoelectron spectroscopy and simulated using density functional theory (DFT), *ab initio* thermodynamics, and charge transfer estimates. Our DFT calculation results suggest that the model β-Mo_2C (011) surface favors the adsorption of O* from water during the electrochemical oxidation, giving rise to the anodic current. Oxygen atoms preferentially interact with surface C sites, forming stable −C═O species and oxycarbide-like surfaces. Highly oxidized surfaces become kinetically unstable and undergo a deeper, substitutional oxidation through −C═O replacement by O*, forming a thermodynamically stable Mo(IV) surface oxide, where each Mo atom coordinates with up to six O atoms. The rate-limiting step switches from CO desorption, occuring within the potential window from 0.28 to 0.51 V, to water dissociation above 0.51 V. The computational results agree well with experimental observations, such as the onset potential (0.6 V) for rapid surface oxidation. This work helps to unravel the details of evolution of surface sites during an oxidation process of molybdenum carbides along with their effects on catalytic properties and lays the foundation for their practical use in various applications.

Received 14th March 2024
Accepted 15th May 2024

DOI: 10.1039/d4ta01746c

rsc.li/materials-a

1. Introduction

Early transition metal carbides (TMCs) are promising substitutes for heterogeneous noble metal catalysts in water splitting,[1–3] nitrogen reduction,[4,5] and biomass conversion,[6,7] as well as in more traditional petrochemical processes such as isomerization, deoxygenation, and hydrogenation. Their platinum-like catalytic properties stem from the interstitial insertion of carbon atoms into the lattice of transition metals, which leads to orbital hybridization and brings about the d-band electronic density of states at the Fermi level resembling noble metals.[8,9] Bulk TMCs may exhibit thermal stability, mechanical strength, outstanding hardness, and corrosion resistance, which in principle make them less likely to suffer from metal leaching in aqueous electrolytes in comparison with metal and alloy electrocatalysts.[10,11] Making low-cost, durable, and electroactive materials for electrodes has become an important part of the commercialization of electrolyzers in recent years. In this context, various TMC materials have been explored as cathodic electrocatalysts for the hydrogen evolution reaction (HER), thanks to their distinct phases and various compositions.[12–16] They also serve as novel substrates for transition metal catalysts, including noble metals.[17–21] With the advancement in nanoengineering methods which are supported by computational methods, structure designs have become critical in studying the surface active sites and reaction mechanisms.[22–25]

Department of Chemical and Biomolecular Engineering, University of Illinois Urbana-Champaign, 600 S. Mathews Ave., Urbana, IL, 61801, USA. E-mail: alexmir@illinois.edu; hy66@illinois.edu

† Electronic supplementary information (ESI) available: Micrographs, cyclic voltammetry curves, polarization curves, capacitance measurement, XPS data and analysis, and notes for DFT and *ab initio* thermodynamics calculations. See DOI: https://doi.org/10.1039/d4ta01746c

The effect of surface oxidation of metal carbides on electrocatalytic activity, however, has not been examined carefully, leaving uncertainty in understanding kinetics for various reactions. Early TMCs, especially those in the nanoscale that are relevant to catalysis, are inevitably oxidized under ambient conditions, resulting in a change of catalytic activity. Partially oxidized surfaces of metal carbides possess both oxygen-modulated, metallic-like H-adsorption sites and Brønsted acid hydroxyl sites.[26] The coexistence of diverse active sites offers unique opportunities for creating multifunctional catalysts whose properties can be tuned according to the degree of surface oxidation. For example, processing with oxygen allows for facile *in situ* control of acidic sites on 2–5 nm Mo_2C crystallites, where the site densities were reversibly changed by a factor of ~30.[27] The oxygenated molybdenum carbides were reported to exhibit different product selectivity in hydrodeoxygenation and dehydrogenation reactions.[28–32] Controlled oxidation thus plays a pivotal role in determining the relative concentrations of distinct active sites, which might result in completely different reaction pathways.[33] Despite much interest and attempt, there are few reports on method development for controlling the surface oxidation and detailed studies of its impact on catalysis. An insight into controlled oxidation and its relationship with catalytic properties is particularly important for state-of-the-art applications of TMCs in the HER, nitrogen reduction reaction (NRR), and biomass conversion,[34–38] just to name a few.

In this work, we used an electrochemical approach in the surface treatment of β-Mo_2C electrocatalysts and carefully examined the effect of surface oxidation on the electrocatalytic properties towards the HER. The hydrogen evolution reaction is chosen because of its sensitivity to the surface structures and its crucial role in the production of green hydrogen. We choose to use electrochemical oxidation of hexagonal phase β-Mo_2C because this process is expected to irreversibly oxidize carbide surfaces at an electrode potential above 0.4 V (*vs.* NHE).[39] Controlled surface oxidation of β-Mo_2C was carried out in an acidic aqueous electrolyte and monitored by cyclic voltammetry (CV). Compared with direct oxidation in air, electrochemical oxidation is largely confined to the surface of electrodes; thus, the degree of oxidation can be controlled by the applied potential window. In this study, for as-prepared β-Mo_2C electrocatalysts, the onset potential of electrochemical oxidation was found to be ~0.6 V (*vs.* RHE, unless otherwise stated) and the current density reached the maximum at ~0.8 V. The oxidized β-Mo_2C electrocatalysts exhibited lowered HER activity with the increased degree of oxidation. The spectroscopic data indicate surface oxycarbide formation upon deposition of oxygen atoms on exposed surface sites at potentials below 0.4 V. Density functional theory (DFT) and *ab initio* thermodynamics calculations indicate that oxygen atoms preferentially interact with surface carbon atoms to form oxycarbide-like surfaces. The rate-limiting step for oxidation also switches from CO removal at a low potential range up to 0.51 V to water dissociation at a higher treatment potential. At a potential above 0.6 V, the surface undergoes further oxidation to form Mo(IV) and Mo(VI) species. The oxidation trends agree surprisingly well between experimental observations and computational predictions. Surface metal oxide phases exhibited considerably lower HER activity than those of metal oxycarbides.

2. Experimental

2.1 Materials

Ammonium molybdate (*para*) tetrahydrate ($(NH_4)_6Mo_7O_{24}\cdot 4H_2O$, 99.9%) was obtained from Alfa Aesar. Ketjen black EC300J was purchased from Akzo Nobel. Methane (CH_4, UHP), hydrogen (H_2, UHP), nitrogen (N_2), compressed air (breathing quality grade), and argon (Ar, UHP) were obtained from Airgas Inc. Ethanol (190 proof) was bought from Decon Lab, Inc. Nafion 117 solution (~5% in a mixture of lower aliphatic alcohols and water) was purchased from Sigma-Aldrich. Formic acid (HCOOH, 70% Veritas double distilled) and perchloric acid ($HClO_4$, 70% Veritas double distilled) were obtained from GFS Chemicals. All chemicals and reagents were used as received without treatment.

2.2 Synthesis of carbon-supported β-Mo_2C

Carbon-supported β-Mo_2C was prepared using the wet impregnation method, followed by a carburization step. In a typical synthesis, $(NH_4)_6Mo_7O_{24}\cdot 4H_2O$ (756 mg) and carbon black (243 mg) were mixed with 20 mL of deionized (DI) water (Millipore, resistivity of 18.25 MΩ cm) in a 100 mL flask. The mixture was then heated on a hotplate stirrer (VWR 7 × 7 Ceramic Hotplate Stirrer 97042-714) at 70 °C (500 rpm) in an oil bath overnight to evaporate most of the water. The remaining solids were transferred to a vacuum oven (VWR Symphony Vacuum Oven, cat. no. 414004-582) and dried at 60 °C for half an hour. The dried solids were ground into a fine powder and loaded into a quartz tube, which was placed in a vertical furnace. The quartz tube was air-tight and was filled with a flowing gas mixture of CH_4/H_2 (flow rate ratio: 8/32; 40 sccm in total). The heating of the furnace was programmed to first increase to 300 °C at a rate of 4 °C min^{-1} and then increase to 650 °C at a rate of 1 °C min^{-1}. The temperature was kept at 650 °C for 2 h, followed by a natural cooling process. After the furnace was cooled to room temperature, the quartz tube was purged with N_2 for 10 min and then with 2% O_2 (a mixture of 10 sccm compressed air and 90 sccm N_2) for 1 h (the passivation step).

2.3 Electrochemical oxidation of carbon-supported β-Mo_2C

A CHI 760E electrochemical workstation was used to carry out all electrochemical measurements. The three-electrode testing system consists of a glassy carbon rotating disk electrode (RDE, Pine Research Instrumentation, 0.196 cm^2 geometric area) as the working electrode, a graphite rod as the counter electrode, and a reversible hydrogen electrode (RHE) as the reference electrode. The controlled electrochemical oxidation was conducted by performing CV in a mixed aqueous electrolyte solution of 0.1 M $HClO_4$ and 0.5 M HCOOH. The solution was purged with Ar for 20 min to remove dissolved oxygen gas. The CV curves were collected in the potential window from −0.025 V

to a predetermined value of 0.4, 0.65, 0.75, 0.85, 0.975, and 1.2 V, respectively. All potentials are *versus* RHE, unless indicated otherwise. The scan rate of CV was 20 mV s^{-1}. The RDE rotation speed was set at 900 rpm. In the preparation of working electrodes, 3 mg of the freshly made β-Mo_2C was dispersed in a mixture of 500 μL of DI water, 1500 μL of ethanol, and 6 μL of Nafion 117 aqueous solution. The typical duration of exposure to air of the as-prepared β-Mo_2C between synthesis and electrochemical measurement was within one week. The mixture was sonicated (2510R-DTH Branson) for 5 min to form a homogeneous suspension (ink). A total volume of 10 μL ink was then drop-cast onto the RDE. The ink-loaded electrodes were then dried in air.

To prepare the oxidized samples under different applied potentials for X-ray photoelectron spectroscopy (XPS), we used carbon paper (catalyst geometric area: 1 × 1 cm^2) instead of the RDE as the working electrode in the electrochemical oxidation step. The catalyst loading per geometric area was kept the same as those in the RDE tests.

2.4 Material characterization

Powder X-ray diffraction (XRD) patterns were obtained using a Rigaku Miniflex 600 diffractometer equipped with a Cu Kα X-ray source (λ = 1.54056 Å). Rietveld refinement of the XRD pattern was conducted using a profile fitting software, TOPAS, provided by Bruker Corporation. The volume-weighted mean crystallite size was calculated from the built-in size estimation functions, based on the refinement results. Transmission electron microscopy (TEM) micrographs were obtained using a JEOL 2100 Cryo microscope. The high-resolution TEM micrographs and energy dispersive X-ray spectroscopy (EDS) elemental mapping images were obtained using a ThermoFisher Scientific Talos F200X G2 Scanning Transmission Electron Microscope (STEM). Thermogravimetric analysis (TGA) was conducted using a Q50 Thermogravimetric Analyzer from TA Instruments. X-ray photoelectron spectroscopy (XPS) data were obtained using a Kratos Axis Supra+ Photoelectron spectrometer. For the preparation of XPS samples, freshly prepared β-Mo_2C was tested in the dry powder form. Oxidized β-Mo_2C samples were loaded on the carbon paper as described in Section 2.3. The XPS analysis was performed by using CasaXPS software. The identification and interpretation of XPS data were based on those provided in the XPS handbook.[40] The principle of spin–orbit splitting ratio for the Mo 3d spectrum, *i.e.*, 2 : 3 for $3d_{3/2}$ and $3d_{5/2}$, was applied when deconvoluting the peaks.

2.5 Electrochemical measurement of catalytic properties

The electrocatalytic activity toward the HER was determined in Ar-saturated 0.1 M $HClO_4$ aqueous electrolyte using the same three-electrode testing system described in Section 2.3. The RDE after the electrochemical oxidation was used as the working electrode. Liner sweep voltammetry (LSV) curves were collected in the potential window between 0 and −0.5 V at the scan rate of 20 mV s^{-1}. The RDE rotation speed was set at 900 rpm.

The electrochemically active surface area (ECSA) was estimated based on double-layer capacitance measurement. The measurement was carried out in Ar-saturated 0.1 M $HClO_4$ aqueous electrolyte using the same three-electrode testing system described in Section 2.3. The CV curves were collected in the potential window between −0.025 and 0.325 V at a scan rate of 10, 20, 30, 40, and 50 mV s^{-1}, respectively. The RDE was kept steady during the measurement. The error bars shown are the standard deviations based on three tests on the same sample.

2.6 Computational method

Spin-polarized periodic density functional theory calculations were performed using the Vienna *ab initio* simulation software (VASP 6.2.0).[41–44] The projector-augmented wave method was used to model core-valence electron interactions[45,46] with a plane-wave cutoff of 450 eV. We employed the PBE[47] exchange-correlation functional with D3[48] corrections for cell and geometry optimizations, followed by single-point, D3-corrected HSE06[49,50] calculations (with HSE-specific D3 parameters)[50] at the optimized PBE geometries. The first Brillouin zone was sampled using a 14 × 14 × 14 Monkhorst–Pack grid[51] for bulk calculations and a 4 × 5 × 1 grid for surface calculations. Initial bulk structures were taken from Shrestha *et al.*[52] for β-Mo_2C ($P6_3/mmc$ space group) and were optimized at our chosen settings, resulting in lattice constants of a = 3.018 Å, b = 3.016 Å, and c = 4.681 Å. These values compare well with the experimental measurements of $a = b$ = 3.002 Å and c = 4.729 Å.[53] The Pymatgen[54] SlabGenerator[55] function was used to build the β-Mo_2C(011)–C-terminated surface, found to be dominant at the nanoscale.[52] We used a 3 × 1 supercell which exposes 6C and 3Mo atoms. Atoms in the bottom half of the slab were fixed at their bulk positions during geometry optimization. Free energies at 298.15 K were obtained by treating all adsorbate degrees of freedom as harmonic. All vibrational frequencies less than 100 cm^{-1} were shifted up to 100 cm^{-1}, according to the prescription by Truhlar *et al.*[56] All geometry manipulations and job submissions were carried out using the ASE package.[57] Transition state energies and geometries were obtained using the climbing-image NEB method[58] and the dimer method,[59] and were confirmed to have one imaginary vibrational frequency. The solvation environment in surface calculations was described using the VASPsol implicit solvent model[60–62] with the default dielectric constant for bulk water. Bader charges[63–65] were computed for surface Mo atoms at various coverages and were converted to oxidation states by recognizing a linear correlation between both properties (see Fig. S1†). Bulk Mo, Mo_2C, and MoO_3 were used as reference systems for Mo(0), Mo(II), and Mo(VI), respectively.

To elucidate the structure and composition of the surface after electrochemical oxidation, we carried out *ab initio* thermodynamics calculations,[66] assuming equilibrium between chemisorbed O* species and bulk water. Under the equilibrium assumption, the history of a sample (*i.e.*, pretreatment) exerts no influence on its final state, making it possible to neglect the passivation pretreatment step in the model. While H_2O can yield several chemisorbed species (O*, OH*, H_2O*, and H*), the

scope of this computational study is restricted to O* overlayers, due to the configurational complexity of mixed O*/OH*/H_2O*/H* adlayers. O*-covered surfaces are anticipated to dominate at higher potentials due to the stabilization of proton–electron pairs, resulting in the destabilization of OH* and H* in comparison to O*. Additionally, since H_2O* is a good leaving group that forms relatively weak bonds with transition metal atoms, the presence of H_2O* species is not expected to profoundly affect the electronic properties of the surface, its oxophilicity, and the oxidation extent. Consequently, co-adsorbed H_2O* is neglected in our model. A few exploratory (*i.e.*, non-comprehensive) surface calculations involving OH* and H_2O* were carried out to provide qualitative tests for several hypotheses pertaining to surface structure and stability.

In calculations of the Gibbs free energy of formation of partially oxidized β-Mo_2C(011)–C slabs containing nO* atoms, the following reaction was considered:

$$Mo_xC_y + nH_2O(liq) \leftrightarrow Mo_xC_y|O_n^* + 2n(H^+ + e^-) \quad (1)$$

$$\Delta G_{rxn}^{298.15} = \left(G(Mo_xC_y|O_n^*) - G(Mo_xC_y)\right) - n(G(H_2O) - 2G(H^+ + e^-)) \quad (2)$$

$G(Mo_xC_y)$ was approximated by the electronic energy of a pristine slab. $G(Mo_xC_y|O_n^*)$ contained electronic energy along with O* vibrational contributions to enthalpy and entropy. $G(H_2O)$ was computed for water vapor in the ideal gas state at a temperature of 298.15 K and a saturation pressure of 3169 Pa.[67] No implicit solvation was employed in a DFT calculation of a single H_2O molecule, since the free energy of solvation is already accounted for in the saturation pressure. The computational hydrogen electrode model[68] was used to compute the energy of a proton–electron pair as follows:

$$G(H^+ + e^-) = \frac{1}{2}G(H_2) - k_BT\ln(10)pH - eU_{SHE} \quad (3)$$

where $G(H_2)$ is the Gibbs free energy of H_2 ideal gas at 298.15 K and 101 325 Pa, and U_{SHE} is the electrode potential with respect to the standard hydrogen electrode, determined using $U_{SHE} = U_{RHE} - 0.059$ V. Free energies of molecules used in this work are reported in Table S1.† The pH value of one was used for the entirety of this work. All applied potentials are reported on the RHE scale, unless stated otherwise.

To sample the configurational space in the most computationally efficient way, we adopted the following sequential O* addition procedure. First, we identified the most energetically favorable position of a single O* atom on a pristine β-Mo_2C(011)–C surface, which turned out to be a C site (more favorable than Mo by 0.21 eV at 0 V). Then, keeping the first O* atom fixed, we explored possible configurations for the second O* atom. For the lowest-energy configuration of two O* atoms, the third atom was added at various positions. The sequential approach reduced the search space down to a total of 46 structures. Other computational details can be found in Notes S1–S7 of the ESI.†

3. Results and discussion

3.1 Sample preparation and structural characterization

Powder X-ray diffraction (XRD) analysis was performed to confirm the crystal phase of freshly prepared solid samples. All partially oxidized metal carbide samples used in this study were made after a final passivation step to mildly oxidize the surface before their exposure to the ambient environment.[27,69] [**CAUTION**: Without the passivation, freshly made molybdenum carbide powder samples ignite upon their exposure to ambient air]. The results show that the XRD peaks of the freshly made sample match well with the diffraction pattern of hexagonal phase β-Mo_2C (PDF#35-0787) (Fig. 1a). No extra diffraction peaks were observed, suggesting that the mild oxidation during passivation is limited to the surface and does not affect the bulk phase of metal carbide nanoparticles. The XRD pattern of as-prepared β-Mo_2C did not fit any of the simulated patterns for $(Mo_2C)_xO_y$,[70] ruling out the formation of bulk oxycarbide. It should be noted that the existence of oxycarbide has been confirmed by spectroscopic evidence, though to the best of our knowledge, there is no precise description or experimental confirmation of its atomic structure. The most intense XRD peak observed could be assigned to (101) diffraction of β-Mo_2C, which exhibits a narrower full-width half maximum (FWHM) than those of other diffraction peaks. This result suggests a preferred packing on the (101) facet. The measured intensity ratio of (002) to (101) diffractions is close to 0.7, much higher

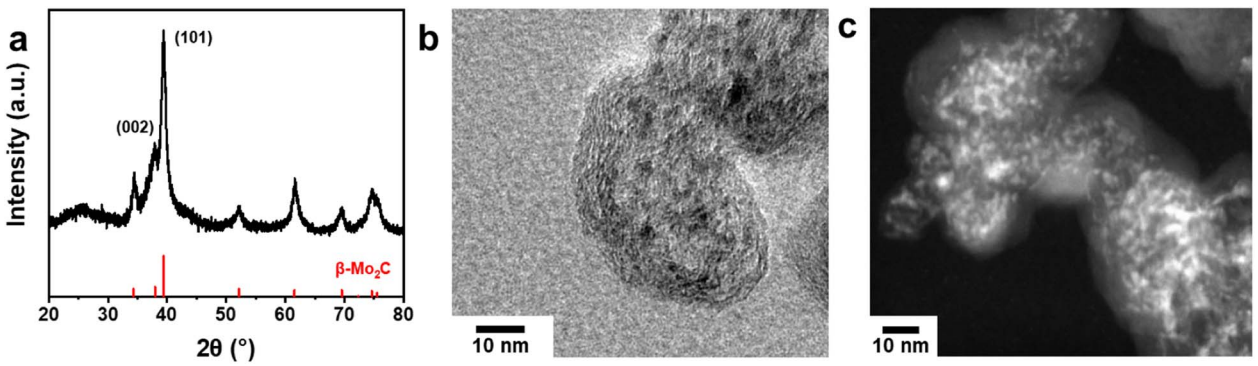

Fig. 1 (a) XRD pattern, (b) TEM micrograph, and (c) dark-field STEM image of as-prepared β-Mo_2C nanoparticles on the carbon support.

than the value of 0.25 in the standard pattern, which implies a disproportionately higher content of (002) packing in the carbide crystals. The volume-weighted mean crystallite size of β-Mo_2C nanoparticles is estimated to be 5.30 ± 0.07 nm, calculated from the Scherrer equation based on the full-profile Rietveld refinement (Fig. S2†).

The TEM micrograph shows the as-prepared β-Mo_2C nanoparticles dispersed across the carbon support (Fig. 1b and S3†). The distribution of β-Mo_2C nanoparticles is more evident in the scanning transmission electron microscope (STEM) micrograph (Fig. 1c). In the dark field TEM, the greyish oval-shaped particle is the carbon support, and the dispersive bright dots indicate regions rich in β-Mo_2C nanoparticles. Energy-dispersive X-ray spectroscopy (EDS) shows the elemental distribution of Mo across the carbon support, which further confirms the formation of well distributed molybdenum carbide nanoparticles (Fig. S4†). We performed TGA to estimate the mass percentage of Mo_2C in the freshly prepared sample, assuming that all Mo atoms exist in the form of Mo_2C. There is 67.5 wt% of MoO_3 in the sample as the combustion product, *i.e.*, the plateau from 580 °C to 700 °C in the weight loss curve (Fig. S5†),[71–73] corresponding to 47.8 wt% of β-Mo_2C in the freshly prepared, carbon-supported sample.

3.2 Electrochemical oxidation and catalytic performance

Controlled surface oxidation of as-prepared β-Mo_2C was monitored by CV in the potential windows between −0.025 V and a predetermined value up to 1.2 V (Fig. 2a). The results indicate the onset potential of oxidation was about 0.6 V and the peak current density was achieved at the forward potential around 0.8 V. The difference between the onset potential (~0.6 V) and the previously reported value (~0.4 V *vs.* NHE) of the carbide planar sheet[39] might be explained by the small size of the as-prepared nanoparticles, which change oxidation kinetics. The CV data show the oxidation current to be close to zero at the forward potential of 1.2 V, suggesting a complete surface oxidation of the metal carbide electrocatalyst. For all CV cycles, the back scans (direction shown by the green arrow in Fig. 2a) do not exhibit any reduction peaks, indicating that the electrochemical oxidation is irreversible. In this study, we name the various electrocatalyst samples as β-Mo_2C-*x*, according to the highest applied potential in V *vs.* RHE used in the electrochemical oxidation process, where *x* is 0.4, 0.65, 0.75, 0.85, 0.975, and 1.2, respectively.

The partially oxidized Mo_2C electrodes were tested for their HER activity by LSV (Fig. 2b). The HER performance of freshly prepared β-Mo_2C was measured for comparison (Fig. S6†). The polarization curves for β-Mo_2C-0.4 and β-Mo_2C-0.65 overlap with each other, suggesting similar HER catalytic properties for samples treated under these two different potential windows. For β-Mo_2C-*x* (x = 0.75, 0.85, 0.975, and 1.2), the HER current densities decreased at a given potential with the increase of upper limit potential value *x*, indicating that the surface oxidation of β-Mo_2C catalysts is detrimental to the HER activity.

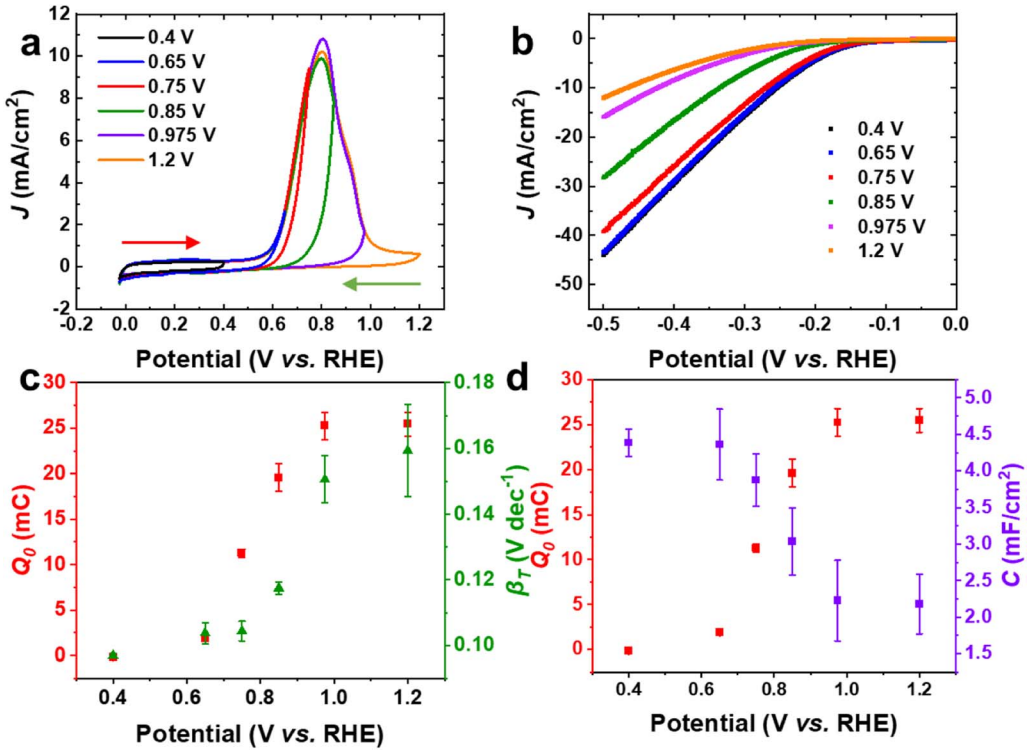

Fig. 2 Structure–property relationships of surface-oxidized β-Mo_2C electrocatalysts towards the HER. (a) CV curves recorded during the electrochemical surface oxidation (red arrow: direction of the forward scan; green arrow: direction of the back scan). (b) Polarization curves of surface oxidized β-Mo_2C-*x* electrocatalysts for the HER. (c) Relationship between total oxidation charges (Q_0) and Tafel slopes (β_T). (d) Relationship between total oxidation charges and capacitance (C).

We carried out a semi-quantitative analysis of surface oxidation and the HER activity relationship based on the CV and the LSV. In our treatment, the degree of surface oxidation is related directly to the total number of electrons withdrawn from the sample surface during the electrochemical oxidation. The total number of oxidation charges (Q_0) was obtained as the integral of current over time, that is, $Q_0 = \int I dt$, where t is the time and I is the total current. Thus, the higher the value of Q_0, the higher the degree of oxidation. Our data indicate that the surface of β-Mo_2C-1.2 should be fully oxidized after the treatment since no oxidation current could be observed at 1.2 V by CV. The fully oxidized nature was also confirmed by the close-to-zero current density after the second and third treatments, monitored by CV (Fig. S7†). The HER polarization curves were further examined by performing Tafel analysis. Tafel slopes (β_T) around the onset potential, *i.e.*, where the current density reached 1 mA cm^{-2}, were calculated. The obtained values are summarized in Table 1.

Fig. 2c shows the Q_0 values as a function of the upper limit potential used for making surface-oxidized samples. Both Q_0 and β_T exhibit an S-shaped curve from 0.4 to 1.2 V. The curvature reaches the maximum for the samples made at the oxidation potential of around 0.8 V. This is consistent with the highest current density, *i.e.*, the fastest reaction rate of surface oxidation, as shown in Fig. 2a. Since Tafel slope is a kinetic parameter, its increase as a function of surface oxidation suggests that either the number of active sites was reduced, or these surface sites were deactivated. The experimental data indicate that the kinetically sluggish rate-determining step of the HER is associated with those oxygen-incorporated surface sites. However, these surface sites were still HER active, since even β-Mo_2C-1.2 exhibited a current density over 10 mA cm^{-2} at the potential of −0.5 V. The ECSA value could be estimated based on the analysis of double layer capacitance (C) (Fig. 2d and S8–S10†). The change of capacitance follows an inverted S-shape and reaches a plateau with the Mo_2C electrode having the highest degree of surface oxidation.

3.3 Spectroscopic study of oxidized β-Mo_2C

X-ray photoelectron spectroscopy was performed to examine the evolution of surface compositions of as-prepared and surface-oxidized β-Mo_2C-x electrocatalysts (Table S2†).[40] All XPS data were analyzed after the calibration using the adventitious C 1s peak binding energy (BE) value of 284.8 eV. Fig. 3 shows the XPS survey scan, Mo 3d, C 1s, and O 1s for as-prepared β-Mo_2C, β-Mo_2C-0.4, and fully oxidized β-Mo_2C-1.2, respectively. Our XPS survey scan shows that the surface of as-prepared β-Mo_2C contains oxygen, molybdenum, and carbon (Fig. 3a). The oxygen peaks were observed because of the passivation in 2% O_2. Three valence states were identified for Mo based on its 3d XPS peaks: Mo(VI) at 235.9 eV ($3d_{3/2}$) and 233.0 eV ($3d_{5/2}$), Mo(IV) at 232.4 eV ($3d_{3/2}$) and 229.8 eV ($3d_{5/2}$), and Mo(II) at 232.7 eV ($3d_{3/2}$) and 228.8 eV ($3d_{5/2}$) (Fig. 3b).[40] This result indicates that at least three kinds of Mo-based species co-exist in the surface nanostructures, which may include MoO_3, MoO_2, and Mo_2C. The C–Mo bond could be confirmed with the metal carbide peak at 283.4 eV in the C 1s spectrum (Fig. 3c). In the O 1s region, the O–C peak at 532.0 eV is more intense than the O–Mo peak at 530.6 eV, which could be a result of the carbon support in the sample or a preferable O deposition on carbon-terminated sites rather than Mo-terminated sites in the carbides (Fig. 3d). Thus, for passivated, as-prepared β-Mo_2C without electrochemical oxidation, there might be exposed metallic sites on the surface. Such samples also had higher HER current density than any of the electrochemically oxidized samples (Fig. S6†). This experimental result is consistent with our computational results that two third of surface Mo sites are predicted to remain exposed (Section 3.4.1). In the survey scan of β-Mo_2C-0.4, the strong F peaks come from Nafion used in the preparation of ink (see Section 2.3) (Fig. 3e). It appears that Mo(II) peaks of β-Mo_2C-0.4 are much weaker than those of as-prepared β-Mo_2C (Fig. 3f). Meanwhile, there is no C–Mo peak at 283.4 eV in the C 1s region (Fig. 3c and g). Instead, the deconvolution analysis suggests a weak peak centered at 286.7 eV. Such variations in both Mo 3d and C 1s peaks indicate significant changes of surface compositions in these samples. This observation does not mean the new surface sites were deactivated due to further surface oxidation, because the HER activity only got slightly lower for the β-Mo_2C-0.4 sample (Fig. 2b and S6†). In addition, in the Mo 3d region of β-Mo_2C-0.4 (Fig. 3f), the Mo(IV) peak shifted to a lower energy of 229.3 eV ($3d_{5/2}$), representing a −0.5 V shift in BE, compared with that shown in Fig. 3b. Such a BE change of Mo indicates that the valence state is likely between Mo(II) and Mo(IV). Simultaneously, the C 1s XPS peak shifted from 283.4 eV for C–Mo to 286.7 eV for Mo–C–O (Fig. S11†). This structural change could account for the significant change in XPS for β-Mo_2C-0.4 when compared with that of as-prepared β-Mo_2C, despite there being no significant oxidation current in this potential window (Fig. 2a). The convergent XPS data indicate that the surface Mo–C species were mostly converted into Mo–C–O in the Mo_2C electrocatalyst if the oxidation potential reached 0.4 V. However, the as-assigned Mo–C–O peak of β-Mo_2C-x (x = 0.4, 0.65, 0.75, and 0.85) shifted towards high energy after the oxidation potential reached 0.975 V (Fig. S11†). A drop in the percentage of peak area coincides with the disappearance of Mo(II) in Mo 3d spectra (Fig. 3j and S12n†), indicating a more oxidized surface, such as the C–Mo–O moiety as suggested by the DFT calculations. In the O 1s region of β-Mo_2C-0.4, the peak at 534.2 eV is

Table 1 Results of oxidation charge, Tafel slope, and capacitance of oxidized β-Mo_2C electrocatalysts after treatments under different potential windows

U_{max}[a] (V)	Q_0 (mC)	β_T (mV dec^{-1})	C (mF cm^{-2})
0.4	−0.17 ± 0.04	96.9 ± 0.6	4.39 ± 0.19
0.65	1.9 ± 0.1	103.8 ± 3.3	4.36 ± 0.48
0.75	11.3 ± 0.5	104.4 ± 3.0	3.88 ± 0.36
0.85	19.6 ± 1.5	117.5 ± 2.0	3.04 ± 0.46
0.975	25.2 ± 1.5	150.6 ± 7.2	2.23 ± 0.55
1.2	25.4 ± 1.3	159.3 ± 14.1	2.18 ± 0.41

[a] U_{max} is the highest applied oxidation potential for the electrochemical treatment of β-Mo_2C.

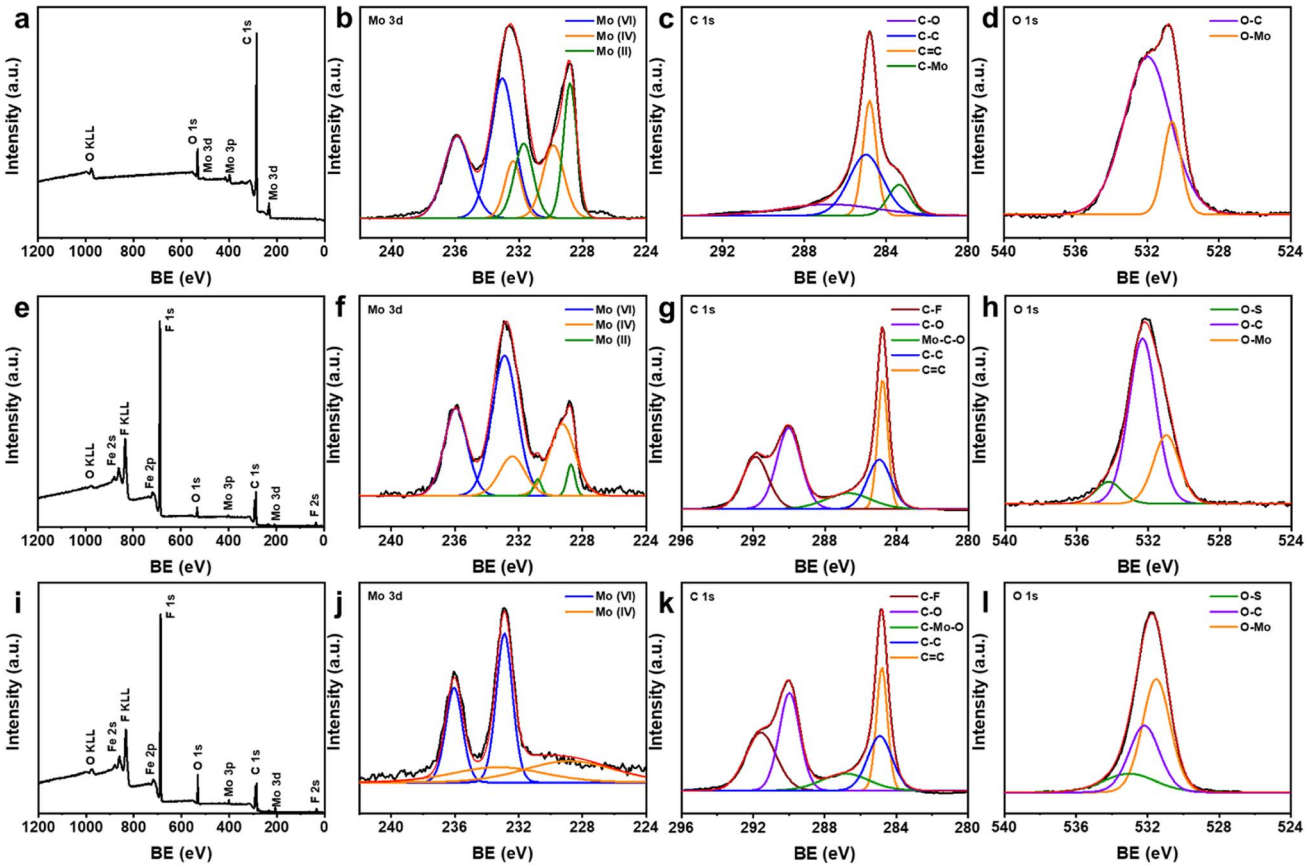

Fig. 3 Survey scan XPS; Mo 3d, C 1s, and O 1s for (a–d) as-prepared β-Mo_2C, (e–h) electrochemically partially oxidized β-Mo_2C-0.4, and (i–l) fully oxidized β-Mo_2C-1.2.

assigned to O–S from Nafion used in the ink (Fig. 3h). No Mo(II) peaks were detected in the Mo 3d region of β-Mo_2C-1.2, and the observed weak peaks could be assigned to Mo(IV), suggesting that this XPS signal may come from the sub-layer Mo atoms (Fig. 3j). There is no major difference in the C 1s XPS peak between β-Mo_2C-1.2 and β-Mo_2C-0.4 (Fig. 3k). However, the XPS signals from O–C and O–Mo suggest that C and Mo react with O differently during the electrochemical oxidation (Fig. 3l).

Besides the comparative analysis of as-prepared, electrochemically partially oxidized (β-Mo_2C-0.4) and fully oxidized (β-Mo_2C-1.2) samples, we further examined Mo 3d, C 1s, and O 1s XPS spectra for the entire series of oxidized samples to understand the detailed surface compositions after different treatments for surface oxidation. The Mo(II) peaks exist throughout the partially oxidized samples that were created at the oxidation potential lower than or equal to 0.85 V ($x = 0.4$, 0.65, 0.75, and 0.85) (Fig. 4a). However, the C 1s spectra of these oxidized β-Mo_2C-x do not exhibit the carbide carbon peak at 283.4 eV (Fig. 3g and S12†). These spectroscopic data suggest the formation of surface oxycarbide once the oxidation potential reaches 0.4 V. The transition from carbide to oxycarbide can explain the disappearance of the carbide C 1s peak of β-Mo_2C-0.4. The strong anodic peak starting at 0.6 V for β-Mo_2C-x ($x >$ 0.4) however suggests a further oxidation event that differs from the aforementioned formation of oxycarbide. Experimentally we observed that the XPS Mo(II) peaks disappeared for β-Mo_2C-0.975 and β-Mo_2C-1.2, indicating that the surface oxycarbide was not stable and further oxidized once the potentials were higher than 0.975 V. Only Mo(IV) and Mo(VI) peaks are observed for β-Mo_2C-0.975 and β-Mo_2C-1.2. The XPS data indicate that MoO_3 is the dominant phase for Mo species on the surface for β-Mo_2C-1.2.

The O 1s XPS data provide additional insights into the change of surface structures for these partially oxidized β-Mo_2C samples, providing information for understanding the interactions between oxygen and surface oxycarbide (Fig. 4b). For β-Mo_2C-x ($x = 0.4$, 0.65, 0.75), XPS O 1s spectra show signals from both O–C and O–Mo, suggesting a competitive chemisorption of oxygen onto surface Mo and C atoms, which is consistent with the existence of surface oxycarbide. When the oxidation potential was raised above 0.75 V, the O–Mo peak began to dominate, suggesting the formation of MoO_x. The relative peak intensity in XPS O 1s between O–C and O–Mo decreased at potentials higher than 0.75 V (Fig. S13†), indicating the elimination of CO_x species, which is explained further based on our computational results (Section 3.4.1).

The XPS data, together with the electrochemical results, thus indicate that the surface may evolve into oxycarbide first and then into oxide after electrochemical treatments under different potential windows. If oxygen interacted with the C-terminated

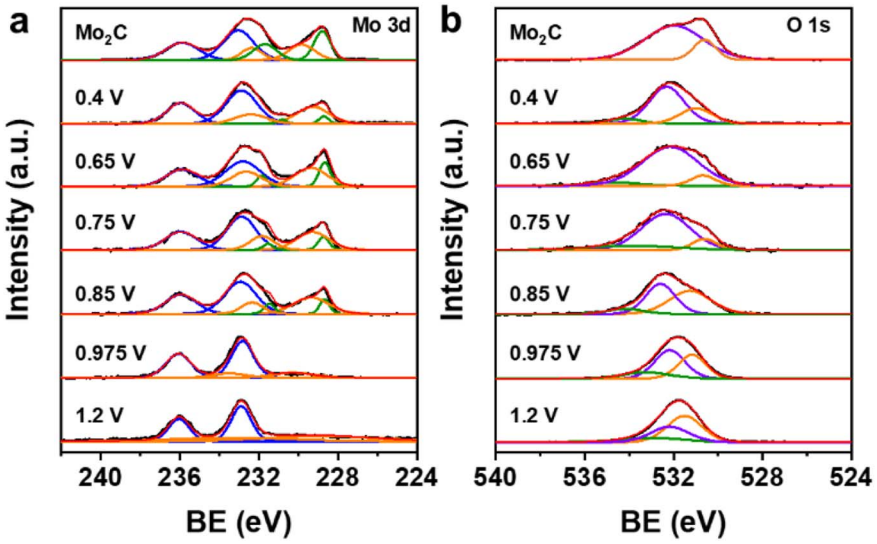

Fig. 4 XPS of β-Mo_2C electrocatalysts in (a) Mo 3d (blue: VI; orange: IV; green: II) and (b) O 1s (green: O–S; violet: O–C; orange: O–Mo) regions, exhibiting evolution of surface compositions as a function of the upper limit of potential used in the electrochemical oxidation process. The black lines are obtained XPS curves and the red lines are fitting envelopes.

surface (Mo–C), an oxycarbide (Mo–C–O) surface formed. The observation of molybdenum oxycarbide (Mo–C–O) fragments in the XPS C 1s region for all oxidized samples indicates this formation pathway (Fig. 3c, g, k and S12†). For Mo-terminated surfaces (C–Mo), XPS data suggest that the Mo–O surface formed as the limit of forward potential increased. The intensity of the O–Mo peak in O 1s XPS of β-Mo_2C-*x* grew when the *x* value changed from 0.75, to 0.85, 0.975, and 1.2, indicating the continuous formation of surface Mo–O species.

3.4 DFT and *ab initio* thermodynamics calculations

3.4.1 Evolution of surface motifs during electrochemical oxidation of β-Mo_2C. Theoretical calculations were carried out to gain insights into the change of atomic structures of the Mo_2C surface after the electrochemical oxidative treatments. Fig. 5 shows the O* surface configurations that are most thermodynamically stable in the potential range of 0 to 0.6 V, along with their free energies. In the range of 0 to 0.28 V, the model predicts the partially oxidized surface to be the most stable, with 1/3 of hollow Mo sites and all exposed C sites covered with O*, denoted as $(Mo–O)_1(C–O)_6$. In this potential window, 2/3 of Mo sites are predicted to remain exposed. Less oxidized surfaces (*i.e.*, $(Mo–O)_0(C–O)_n$, $n = 1$–6) are found to be less thermodynamically stable by more than 1 eV and thus expected not to form at any positive potentials (Fig. 5b). The lowest (most negative) lines correspond to the most stable surfaces at specific potential windows, marked by colored regions. Two hatched regions depict the slow and fast CO/CO_2 removal, respectively, which leads to the C* substitution with O* and the formation of surface oxide. Our simulation indicates that the increase in the applied potential results in further oxidized structures $(Mo–O)_3(C–O)_6$ and $(Mo–O)_4(C–O)_6$, which first appear at 0.28 and 0.51 V, respectively. In $(Mo–O)_3(C–O)_6$, all Mo and C sites are covered with O*, whereas in $(Mo–O)_4(C–O)_6$, an extra oxygen atom brings about surface restructuring through the displacement of C–O. The formation of oxidized surfaces at low potentials is consistent with the C 1s XPS spectrum of β-Mo_2C-0.4, which exhibits both C–O and Mo–C–O oxycarbide features (Fig. 3e–h). Table 2 shows the average Mo oxidation states obtained from calibrated Bader charges (Fig. S1†). For partially oxidized $(Mo–O)_n(C–O)_6$ structures, the Mo oxidation states are close to +2, which corresponds to Mo(II) peaks in XPS data for β-Mo_2C and β-Mo_2C-0.4 (Fig. 3b and f).

The measured Q_0 (the total oxidation charge) values due to the formation of an oxidized surface are consistent with and explained by the computational results (Table 3 and eqn (S12)†). The experimentally determined Q_0 values are closely associated with the change of surface species from $(Mo–O)_1(C–O)_6$ to $(Mo–O)_3(C–O)_6$ and $(Mo–O)_3(C–O)_6$ to $(Mo–O)_4(C–O)_6$, which occur at 0.28 and 0.51 V, respectively, based on the simulation results. The simulated Q_0 values associated with these changes are found to be 1.31 mC at 0.28 V and 0.65 mC at 0.51 V, which are comparable in magnitude to the experimentally obtained values of -0.17 ± 0.04 mC at 0.4 V and 1.9 ± 0.1 mC at 0.65 V (Table 1). The observation that the measured Q_0 at 0.4 V is smaller in magnitude than the predicted one might be due to one of the following factors. The surface after passivation is more oxidized than $(Mo–O)_1(C–O)_6$ and stable at a more positive potential due to the sluggish kinetics for the H_2O/O^* adsorption equilibrium over the timescale of CV measurement. Alternatively, the H_2O/O^* equilibrium may be a kinetically fast step, leading to the fully reversible O* surface deposition. In this scenario, the experimental Q_0 reflects an irreversible oxidation of surface oxycarbide to surface oxide. Further studies discussed below suggest that the irreversible oxidation does not occur to a significant degree below 0.5 V, making it more likely for Q_0 to be reflective of irreversible surface oxide formation.

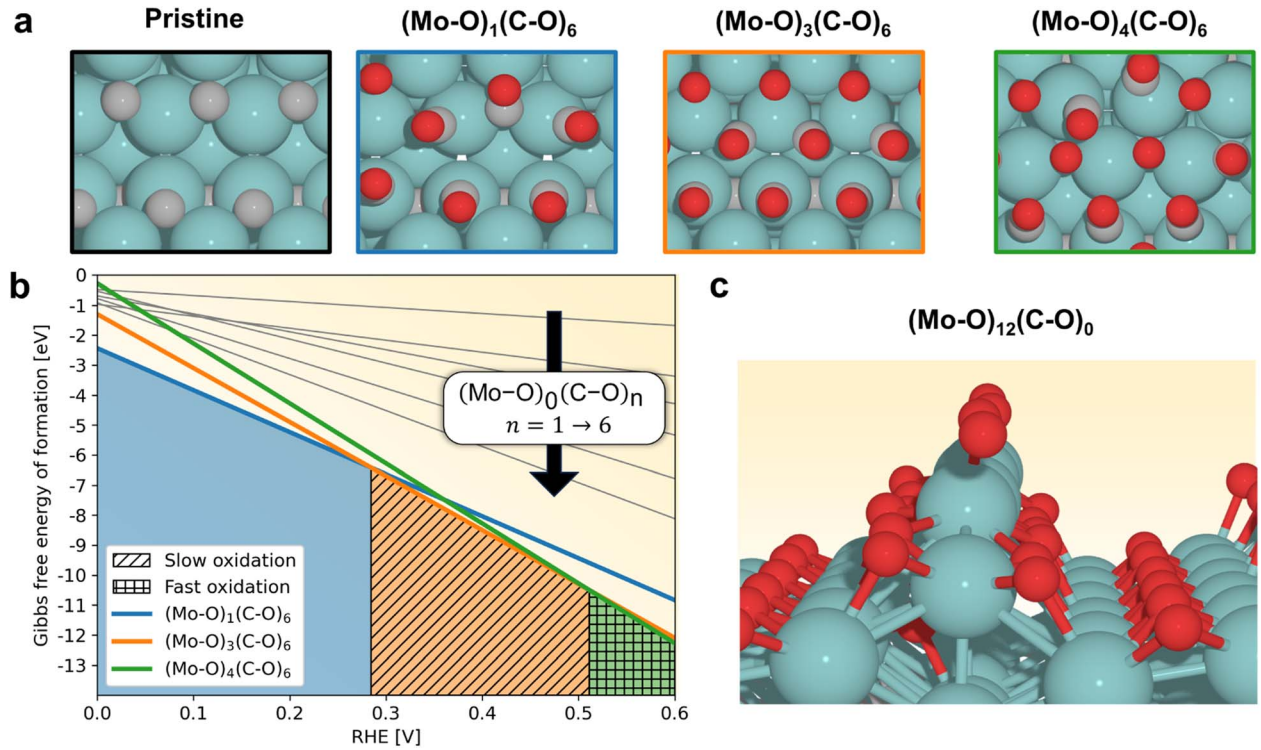

Fig. 5 Thermodynamically stable β-Mo_2C(011) C-terminated surfaces in the potential range of 0 to 0.6 V. (a) Top view of identified structures. The pristine surface is included for reference. (b) Gibbs free energy of formation as a function of applied potential. (c) Proposed surface oxide structure formed after the complete oxidation in hatched regions at a higher potential (cyan: Mo; grey: C; red: O).

Table 2 Average and calibrated Bader charges on surface Mo atoms

Surface	Net atomic Bader charge	Oxidation state
Pristine β-Mo_2C(011)–C	+0.83	+2.21
$(Mo–O)_1(C–O)_6$	+0.71	+1.91
$(Mo–O)_3(C–O)_6$	+0.81	+2.16
$(Mo–O)_4(C–O)_6$	+0.81	+2.16
$(Mo–O)_{12}(C–O)_0$	+1.37	+3.57

Table 3 Estimates of charge transfer values for surface oxidation

Oxidation step	Charge transfer (mC)
$(Mo–O)_1(C–O)_6 \rightarrow (Mo–O)_3(C–O)_6$	1.31
$(Mo–O)_3(C–O)_6 \rightarrow (Mo–O)_4(C–O)_6$	0.65
$(Mo–O)_1(C–O)_6 \rightarrow (Mo–O)_{12}(C–O)_0$	7.19
Replace all C in a nanoparticle to O	45.2

As the $(Mo–O)_4(C–O)_6$ species is predicted to form at 0.51 V, no more exposed surface Mo and C sites are available for reaction with O* following the previously suggested pathway. Thus, the experimentally observed high oxidation currents at potentials above 0.5–0.6 V should come from other sources, namely, the subsurface structures having higher oxygen coverages may involve C* substitution with H_2O-derived O*. In such a process, surface carbon may react and form CO and CO_2 species, which subsequently leave the surface. This surface reaction should result in the formation of vacancies that are filled with oxygen atoms and, as a result, two electrons (along with two H^+) are released per every substituted carbon atom. Indeed, computationally we found that C* substitution for O* is thermodynamically favorable at a wide range of applied positive potentials from 0.05 V to 1.2 V (Note S3†).

Our simulation results further indicate that the computed energy barrier for CO removal is a suitable parameter to evaluate the kinetic stability of oxidized surfaces. The removal of CO is proposed to be the rate-limiting step (RLS) in substitutional oxidation, as the follow-up reoxidation of highly oxophilic vacancies is expected to be fast. Table 4 summarizes the calculated values of kinetic barriers for CO and CO_2 removals on the relevant Mo–C surfaces, agreeing with the substitutional oxidation process at high O* coverages. The HSE level of theory

Table 4 Kinetic barriers for CO and CO_2 removal computed at the HSE level of theory[a]

Surface	CO (eV)	CO_2 (eV)
$(Mo–O)_0(C–O)_6$	1.79 (1.98)	2.58 (2.44)
$(Mo–O)_1(C–O)_6$	1.61 (1.18)	2.75 (2.34)
$(Mo–O)_3(C–O)_6$ type-1	0.73 (0.84)	1.05 (1.11)
$(Mo–O)_3(C–O)_6$ type-2	0.71 (0.83)	1.37 (1.53)
$(Mo–O)_4(C–O)_6$	0.0[b] (0.07)	0.07 (0.07)

[a] Values in parentheses are obtained using the PBE functional. [b] Energy difference came out negative (−0.0071 eV) and thus represented as zero.

calculation reveals CO desorption to be more favorable than CO_2 formation and shows high energy barriers for low-coverage surfaces: 1.79 eV for $(Mo–O)_0(C–O)_6$ and 1.61 eV for $(Mo–O)_1(C–O)_6$ structures, suggesting good kinetic stability. This result is consistent with the predicted lack of a significant current in the relevant thermodynamic stability window of $(Mo–O)_1(C–O)_6$ (0–0.28 V, Fig. 5b). The $(Mo–O)_3(C–O)_6$ structure which is thermodynamically stable within 0.28–0.51 V exhibits a moderate barrier of 0.71 eV and is predicted to undergo substitutional oxidation. In contrast, the CO removal barrier for $(Mo–O)_4(C–O)_6$ which is thermodynamically stable above 0.51 V is found to be very low (0.07 eV or less), indicating that this structure is kinetically unstable and shall rapidly lose CO, resulting in C* substitution with O*, leading to the transformation from metal oxycarbide to oxide on the surface.

Our simulation data also suggest that CO* desorption is no longer the RLS of the substitutional oxidation when the applied potential is above 0.51 V. The corresponding energy barrier on $(Mo–O)_4(C–O)_6$ at 0.51 V is very low and should yield currents much greater than those observed in the experiment (Table S3†). At these potentials, the reaction kinetics is likely limited by the formation of H_2O-derived O*. Our simulation data suggest that H_2O binds weaker to more oxidized surfaces, which shall destabilize the transition states for breaking the O–H bond. For example, the adsorption energy of H_2O changes from −1.06 eV on the exposed Mo atoms of pristine β-Mo_2C(011)–C to −0.1 eV on $(Mo–O)_2(C–O)_6$ and +0.19 eV on $(Mo–O)_3(C–O)_6$, reflecting weak hydrogen bonding and unavailable sites of Mo (Table S4†). Water dissociation, accelerated by the potential,[68] is likely responsible for the 0.1 V shift of the onset potential (0.6 V) from the predicted value (0.51 V) of the oxidation current and attributed to the exponentially rising oxidation current above 0.6 V. It should be noted that lowered onsets of oxidation potential can be obtained in principle. Such reduction in onset potential requires thermodynamic equilibria among $(Mo–O)_n(C–O)_6$ structures that lie closely in energy (Fig. 5b) and a two-step process where the surface is first oxidized, followed by CO* desorption. For example, less oxidized $(Mo–O)_1(C–O)_6$ can undergo substitutional oxidation at potentials as low as ~0.25 V, since kinetically unstable $(Mo–O)_4(C–O)_6$ is only 0.62 eV greater in free energy, resulting in an effective energy barrier of 0.71 eV for the removal of CO. The energy barrier is low enough for the two-step oxidation process to take place on the time scale of tens of seconds, suggesting an exponential increase in current density at potentials above 0.25 V, due to the potential dependence of $(Mo–O)_4(C–O)_6$ formation. This predicted reaction pathway however was not experimentally observed, and the sluggish H_2O dissociation (*vide supra*) likely limits the further oxidation of $(Mo–O)_3(C–O)_6$.

We thus categorize the CO*-desorption and H_2O*-dissociation limited oxidation pathways as the slow and fast substitutional oxidations, respectively (the hatched regions in Fig. 5b). After it is formed at 0.28 V, $(Mo–O)_3(C–O)_6$ experiences slow substitutional oxidation governed by the removal of CO*. At 0.51 V, the formation of kinetically unstable $(Mo–O)_4(C–O)_6$ becomes thermodynamically favorable, which corresponds to fast substitutional oxidation, limited by H_2O dissociation. The

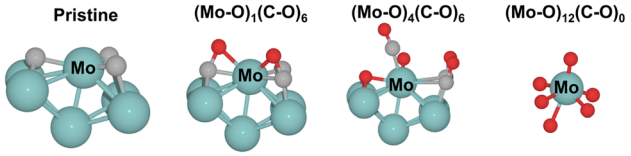

Fig. 6 Illustrations of nearest neighboring atoms for a given Mo at different surface coverages.

slow substitutional oxidation of the $(Mo–O)_3(C–O)_6$ surface should result in the decrease of Mo(II) peaks for the β-Mo_2C-0.4 V sample (Fig. 3b and f). To determine the Mo oxidation state after its substitutional oxidation, we investigated the limiting $(Mo–O)_{12}(C–O)_0$ structure shown in Fig. 5c. Unlike $(Mo–O)_3(C–O)_6$, in which Mo coordinates to Mo, C, and O and adopts the +2 oxidation state, the surface Mo in $(Mo–O)_{12}(C–O)_0$ is only coordinated to O, adopting the +3.57 oxidation state and a distorted octahedral geometry (Mo(IV)) (Fig. 6). Our computational results suggest that the substitutional oxidation results in a progressive change in the Mo oxidation state and chemical environment, which agrees very well with the experimentally observed potential-dependent current density changes that correspond to the surface transformation from metal oxycarbide to oxide. Experimentally, XPS data show a reduced peak area in the Mo(II) region and an increase in Mo(IV) (Fig. 3 and 4).

Compared with computational results based on the substitutional oxidation (Table S3†), the experimentally observed current densities are low for samples made after oxidative treatment below 0.6 V. Our computational and experimental results suggest that two effects might be at play. First, CO* species may be removed and replaced with O* during the passivation step. A large extent of pre-oxidation is supported by the Q_0 "total oxidation" value of 25.4 mC (Table 1), being less than that required to convert the pristine Mo_2C completely to MoO_2 (~45.2 mC), and by the XPS data (Fig. 3). Second, CO* may be protonated and exist in the form of COH* at low potentials, preventing the desorption of CO. Computationally, we found a partially hydroxylated $(Mo–OH)_3(C–OH)_4(C–O)_1$ + H_2O* surface to be very stable thermodynamically across a wide range of potentials up to 0.31 V (Fig. 7). From the comparison of free energies of $(Mo–O)_3(C–O)_6$ and $(Mo–OH)_3(C–OH)_6$ surfaces at 0 V, we expect that deprotonation on average should increase the effective desorption energy of CO by ~0.2 eV. This energy barrier should result in reducing the current density down to ~0.1 mA cm^{-2}, in line with the observed experimental results. Thus, substitutional oxidation should be minor when the potential window for the treatment is below 0.5 V.

3.4.2 Theoretical analysis of the HER catalyzed by partially oxidized β-Mo_2C. The surface oxides formed after substitutional oxidation at above 0.6 V (Fig. 5c) should be stable at negative potential ranges since this electrochemical treatment is irreversible due to the release of gaseous species such as CO and CO_2. This predicted change is consistent with the experimental results, which exhibit no reduction peak during the backward CV scan (Fig. 2a). The polarization curves for HER measurement are relatively stable after 30 cycles of CV scans in the range of

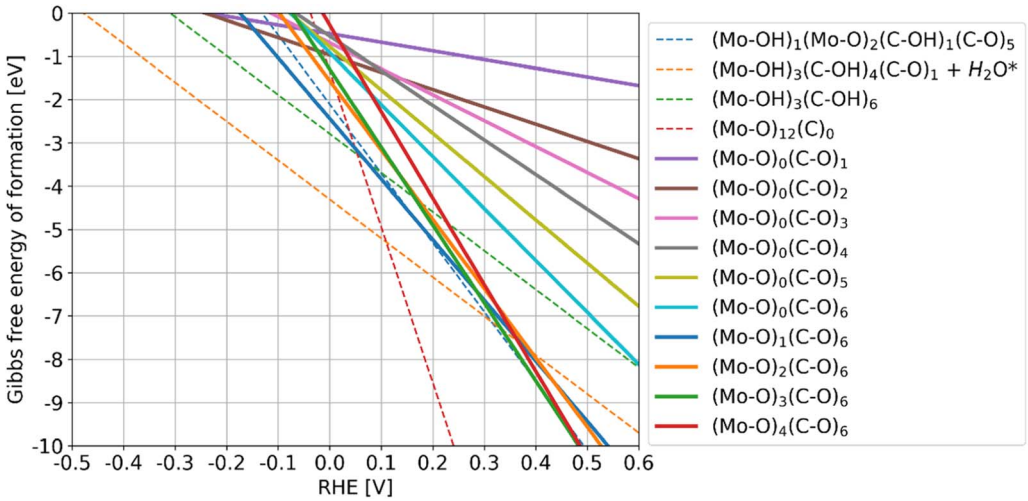

Fig. 7 Gibbs free energy of formation of a range of Mo- and C-containing structures. Solid lines represent energies of $(Mo–O)_n(C–O)_m$ structures where $n = 0–4$ and $m = 1–6$. Dashed lines denote four relevant, special cases of hydroxylated and fully oxidized surfaces.

0 to −0.5 V (*vs.* RHE) (Fig. S14†). Table 2 reports the existence of Mo(IV) in the limiting structure of $(Mo–O)_{12}(C–O)_0$, which corresponds to surface MoO_2. As MoO_2 and MoO_3 exhibit much lower HER activity in comparison with β-Mo_2C,[74,75] the substitutional oxidation leading to the surface oxide should deactivate the carbide surface. Interestingly, β-Mo_2C-1.2 exhibited HER currents closely matching those of MoO_2/MoO_3,[74,75] indicating a complete surface oxidation to MoO_x and the absence of (oxy) carbide features. Higher HER activities observed on less oxidized surfaces ($x < 1$, Fig. 2b) indicate incomplete substitutional oxidation of the surface, and the likely existence of oxycarbide structural motifs that catalyze the HER. Since the charge required to form a surface oxide layer is 7.19 mC, which is less than that of 11.3 mC for U_{max} of 0.75 V and 19.6 mC for 0.85 V, and the HER activity is still significant, bulk oxidation involving subsurface carbons may occur under these conditions.

Unlike the substitutional oxidation, the additive oxidation associated with O* chemisorption below 0.5 V that leads to $(Mo–O)_n(C–O)_m$ structures is reversible (Fig. 5b). Indeed, an Eley–Rideal-type process is feasible, in which O* is protonated to form OH* and then H_2O* at more negative potentials, followed by the desorption of water molecules. The computationally predicted reversibility is consistent with the lack of hysteresis on CV in the potential window of 0–0.4 V (Fig. 2a). It also explains the similarity in HER activity between as-prepared β-Mo_2C and β-Mo_2C-0.4 (Fig. 2b). Thus, both $(Mo–O)_1(C–O)_6$ and $(Mo–O)_3(C–O)_6$ surfaces, predicted to form below 0.28 and 0.51 V, respectively, likely undergo further conversion during the HER at negative U to the same catalytically active surface.

Our thermodynamic calculations also shed light on the state of the surface at negative potentials. Without protonation, the $(Mo–O)_1(C–O)_6$ structure which is stable at U of 0 V loses some oxygen to form $(Mo–O)_0(C–O)_2$ below −0.15 V (Fig. 7). With protonation, O* reacts with proton–electron pairs to form OH*. This process stabilizes greatly chemisorbed oxygen, forming a surface with mixed OH* and H_2O* at the reducing potentials (Fig. 7). The H_2O-absorbed $(Mo–OH)_3(C–OH)_4(C–O)_1$ configuration is particularly stable. The Mo-bound H* is likely present as well (*vide infra*). All such species are expected to be further stabilized through hydrogen bonding. Formation of oxygen vacancies is likely inhibited, and the surface remains stable during the anodic electrochemical treatment of the catalyst.

We further analyzed the nature of the active site towards the HER once the hydroxylated surface is formed at a negative potential. Under such conditions, the HER is expected to occur on the sites of Mo*/C–O* pairs. Water dissociation on a neighboring Mo site coupled with an H diffusion from a neighboring C–OH* yields a stable Mo–H*/C–OH* intermediate, followed by the removal of H_2. In this mechanism, H_2 release is expected to be facile, since its transition state is stabilized through the interaction with a frustrated Lewis acid/base pair of Mo*–O*, and Mo and O are oppositely charged. A similar mechanism in the reverse process (H_2 dissociation) has been proposed on metal oxide surfaces.[76,77] As the formation free energies of H_2O-derived intermediates on Mo sites rank as H* < H_2O* < OH* < O* at 0 V, corresponding to ΔG of −1.12, −1.06, −0.64, and −0.47 eV, respectively, on a pristine surface, we anticipate that surface Mo–OH* motifs recombine to form weakly bound H_2O* which is then replaced by H* (Table S5†). Thus, the formation of Mo–H*/C–OH* is expected to be thermodynamically favorable.

4. Conclusion

In this study, we semi-quantitatively elucidated the important effects of surface oxidation of the β-Mo_2C electrocatalyst on the HER. We achieved a varied degree of surface oxidation using an electrochemical treatment performed under different potential windows. The convergent experimental and computational data point to a reaction pathway in which surface oxidation occurs through C first and then Mo oxidation when the upper limit of the potential window increases. There is also a good agreement between theory and experiment on the exposed sites and their activities for partially or fully oxidized Mo_2C electrocatalysts.

Specifically, XPS data suggest the formation of surface oxycarbide due to the incorporation of oxygen in carbide-terminated surface sites at low potentials (~0.4 V) and the formation of surface Mo(VI) oxide at the final state. Tafel slope and double-layer capacitance analyses indicate that surface oxidation should negatively affect the HER performance.

Computationally, DFT and *ab initio* thermodynamics calculations unveil substantial amounts of H_2O-derived oxygen on all electrochemically treated surfaces of β-Mo_2C electrocatalysts. Two mechanisms dominate the surface oxidation in the electrochemical processes: a reversible additive oxidation through O* chemisorption (<0.51 V) and an irreversible substitutional C*-to-O* oxidation with the concomitant loss of CO (>0.51 V). The substitutional oxidation is associated with a pronounced anodic current at 0.6 V, the formation of a Mo(IV) surface oxide, and a subsequent decline in the HER activity at negative potentials. The additive oxidation yields Mo(II) oxycarbide structures that expose C=O groups and readily react with proton–electron pairs. Protonation favors the surface oxidation and is expected to stabilize the surface against the loss of gaseous oxidative C species. Surface hydroxyls readily recombine and expose Mo*/C–O*, which are proposed to function as frustrated Lewis acid/base pairs and catalyze the HER. This work helps to unravel the effect of surface oxidation on catalytic properties and paves the way for developing practical use of molybdenum carbides in a range of reactions.

Author contributions

S. Y. conceptualization, methodology, writing – original draft, writing – review & editing, data curation, validation, analysis. A. K. G. data curation, writing – original draft, writing – review & editing. D. G. conceptualization, methodology, data curation A. N. K. data curation. H. H. data curation. A. V. M. supervision, conceptualization, methodology, investigation, resources, funding acquisition, writing – original draft, writing – review & editing. H. Y. supervision, conceptualization, investigation, resources, funding acquisition, writing – review & editing.

Conflicts of interest

The authors declare no competing financial interest.

Acknowledgements

This work was supported in part by the National Science Foundation (CBET-2055734 to HY and DMREF-2323988 to AM), and University of Illinois Urbana-Champaign (UIUC). Electron microscopy characterization and X-ray photoelectron spectroscopy were carried out at the Frederick Seitz Materials Research Laboratory Central Research Facilities, UIUC. The X-ray diffraction was carried out at the George L. Clark X-ray Facility and 3M Materials Laboratory, School of Chemical Science (SCS) at UIUC. S. Y. is grateful for a Chia-Chen Chu Fellowship from the SCS.

Notes and references

1 X. Zhang, C. Shi, B. Chen, A. N. Kuhn, D. Ma and H. Yang, *Curr. Opin. Chem. Eng.*, 2018, **20**, 68–77.
2 S. Sun, Y. Liu, G. Xu, C. Jiang, J. Li, L. Fan and W. Cai, *Fuel*, 2023, **335**, 127084.
3 Z. Zhou, Y. Jia, Q. Wang, Z. Jiang, J. Xiao and L. Guo, *Sustainability*, 2023, **15**, 14556.
4 B. Izelaar, D. Ripepi, S. Asperti, A. I. Dugulan, R. W. A. Hendrikx, A. J. Böttger, F. M. Mulder and R. Kortlever, *ACS Catal.*, 2023, **13**, 1649–1661.
5 R. Zhao, Y. Chen, H. Xiang, Y. Guan, C. Yang, Q. Zhang, Y. Li, Y. Cong and X. Li, *ACS Appl. Mater. Interfaces*, 2023, **15**, 6797–6806.
6 S. Zhang, J. Wang, L. Ye, S. Li, Y. Su and H. Zhang, *Chem. Eng. J.*, 2023, **454**, 140072.
7 J. Pang, J. Sun, M. Zheng, H. Li, Y. Wang and T. Zhang, *Appl. Catal., B*, 2019, **254**, 510–522.
8 J. R. Kitchin, J. K. Nørskov, M. A. Barteau and J. G. Chen, *Catal. Today*, 2005, **105**, 66–73.
9 Q. Gong, Y. Wang, Q. Hu, J. Zhou, R. Feng, P. N. Duchesne, P. Zhang, F. Chen, N. Han, Y. Li, C. Jin, Y. Li and S.-T. Lee, *Nat. Commun.*, 2016, **7**, 13216.
10 L. G. Hernández-Maya, I. Zapata-Peñasco, M. Olivares-Luna, I. Campos-Silva, J. Martínez-Trinidad, L. G. Díaz-Barriga, J. N. Rivera-Olvera and V. Garibay-Febles, *Surf. Coat. Technol.*, 2023, **469**, 129816.
11 J. Xu, Z. Li, S. Xu, P. Munroe and Z.-H. Xie, *J. Power Sources*, 2015, **297**, 359–369.
12 C. Wan, Y. N. Regmi and B. M. Leonard, *Angew. Chem., Int. Ed.*, 2014, **53**, 6407–6410.
13 C. Tang, H. Zhang, K. Xu, Q. Zhang, J. Liu, C. He, L. Fan and T. Asefa, *J. Mater. Chem. A*, 2019, **7**, 18030–18038.
14 H. Lin, Z. Shi, S. He, X. Yu, S. Wang, Q. Gao and Y. Tang, *Chem. Sci.*, 2016, **7**, 3399–3405.
15 X. Zhang, J. Wang, T. Guo, T. Liu, Z. Wu, L. Cavallo, Z. Cao and D. Wang, *Appl. Catal., B*, 2019, **247**, 78–85.
16 P. Yin, H. Cai, X. Zhang, B. Chen, Y. Liu, R. Gao and C. Shi, *New J. Chem.*, 2021, **45**, 10396–10401.
17 L. Lin, W. Zhou, R. Gao, S. Yao, X. Zhang, W. Xu, S. Zheng, Z. Jiang, Q. Yu, Y.-W. Li, C. Shi, X.-D. Wen and D. Ma, *Nature*, 2017, **544**, 80–83.
18 S. Yao, X. Zhang, W. Zhou, R. Gao, W. Xu, Y. Ye, L. Lin, X. Wen, P. Liu, B. Chen, E. Crumlin, J. Guo, Z. Zuo, W. Li, J. Xie, L. Lu, C. J. Kiely, L. Gu, C. Shi, J. A. Rodriguez and D. Ma, *Science*, 2017, **357**, 389–393.
19 X. Zhang, M. Zhang, Y. Deng, M. Xu, L. Artiglia, W. Wen, R. Gao, B. Chen, S. Yao, X. Zhang, M. Peng, J. Yan, A. Li, Z. Jiang, X. Gao, S. Cao, C. Yang, A. J. Kropf, J. Shi, J. Xie, M. Bi, J. A. van Bokhoven, Y.-W. Li, X. Wen, M. Flytzani-Stephanopoulos, C. Shi, W. Zhou and D. Ma, *Nature*, 2021, **589**, 396–401.
20 Z. Li, Z. Qi, S. Wang, T. Ma, L. Zhou, Z. Wu, X. Luan, F.-Y. Lin, M. Chen, J. T. Miller, H. Xin, W. Huang and Y. Wu, *Nano Lett.*, 2019, **19**, 5102–5108.

21 D. A. Kuznetsov, Z. Chen, P. V. Kumar, A. Tsoukalou, A. Kierzkowska, P. M. Abdala, O. V. Safonova, A. Fedorov and C. R. Müller, *J. Am. Chem. Soc.*, 2019, **141**, 17809–17816.
22 G.-Q. Yu, B.-Y. Huang, X. Chen, D. Wang, F. Zheng and X.-B. Li, *J. Phys. Chem. C*, 2019, **123**, 21878–21887.
23 L. Zhao, H. Yuan, D. Sun, J. Jia, J. Yu, X. Zhang, X. Liu, H. Liu and W. Zhou, *Nano Energy*, 2020, **77**, 105056.
24 X. Yang, J. Cheng, X. Yang, Y. Xu, W. Sun and J. Zhou, *Chem. Eng. J.*, 2023, **451**, 138977.
25 C. Yang, R. Zhao, H. Xiang, J. Wu, W. Zhong, X. Li and Q. Zhang, *Nano Energy*, 2022, **98**, 107232.
26 M. M. Sullivan and A. Bhan, *J. Catal.*, 2016, **344**, 53–58.
27 M. M. Sullivan, J. T. Held and A. Bhan, *J. Catal.*, 2015, **326**, 82–91.
28 M. M. Sullivan and A. Bhan, *J. Catal.*, 2018, **357**, 195–205.
29 A. Kumar and A. Bhan, *Chem. Eng. Sci.*, 2019, **197**, 371–378.
30 E. A. Blekkan, C. Pham-Huu, M. J. Ledoux and J. Guille, *Ind. Eng. Chem. Res.*, 1994, **33**, 1657–1664.
31 K. Murugappan, E. M. Anderson, D. Teschner, T. E. Jones, K. Skorupska and Y. Román-Leshkov, *Nat. Catal.*, 2018, **1**, 960–967.
32 A. N. Kuhn, R. C. Park, S. Yu, D. Gao, C. Zhang, Y. Zhang and H. Yang, *Carbon Future*, 2024, **1**, 9200011.
33 J. A. Schaidle, J. Blackburn, C. A. Farberow, C. Nash, K. X. Steirer, J. Clark, D. J. Robichaud and D. A. Ruddy, *ACS Catal.*, 2016, **6**, 1181–1197.
34 B. Zhang, J. Zhou, S. R. Elliott and Z. Sun, *J. Mater. Chem. A*, 2020, **8**, 23947–23954.
35 H. Cheng, L.-X. Ding, G.-F. Chen, L. Zhang, J. Xue and H. Wang, *Adv. Mater.*, 2018, **30**, 1803694.
36 Q. Li, S. Qiu, L. He, X. Zhang and C. Sun, *Phys. Chem. Chem. Phys.*, 2018, **20**, 23338–23343.
37 X. Qu, L. Shen, Y. Mao, J. Lin, Y. Li, G. Li, Y. Zhang, Y. Jiang and S. Sun, *ACS Appl. Mater. Interfaces*, 2019, **11**, 31869–31877.
38 X. Du, R. Zhang, D. Li, C. Hu and H. Garcia, *J. Energy Chem.*, 2022, **73**, 68–87.
39 E. C. Weigert, D. V. Esposito and J. G. Chen, *J. Power Sources*, 2009, **193**, 501–506.
40 J. F. Moulder, W. F. Stickle, P. E. Sobol and K. D. Bomben, *Handbook of X-Ray Photoelectron Spectroscopy*, Perkin-Elmer Corporation, United States of America, 1992.
41 G. Kresse and J. Furthmüller, *Comput. Mater. Sci.*, 1996, **6**, 15–50.
42 G. Kresse and J. Furthmüller, *Phys. Rev. B: Condens. Matter Mater. Phys.*, 1996, **54**, 11169–11186.
43 G. Kresse and J. Hafner, *Phys. Rev. B: Condens. Matter Mater. Phys.*, 1994, **49**, 14251–14269.
44 G. Kresse and J. Hafner, *Phys. Rev. B: Condens. Matter Mater. Phys.*, 1993, **47**, 558–561.
45 G. Kresse and D. Joubert, *Phys. Rev. B: Condens. Matter Mater. Phys.*, 1999, **59**, 1758–1775.
46 P. E. Blöchl, *Phys. Rev. B: Condens. Matter Mater. Phys.*, 1994, **50**, 17953–17979.
47 J. P. Perdew, K. Burke and M. Ernzerhof, *Phys. Rev. Lett.*, 1996, **77**, 3865–3868.
48 S. Grimme, J. Antony, S. Ehrlich and H. Krieg, *J. Chem. Phys.*, 2010, **132**, 154104.
49 A. V. Krukau, O. A. Vydrov, A. F. Izmaylov and G. E. Scuseria, *J. Chem. Phys.*, 2006, **125**, 224106.
50 Github, *The D3 Dispersion Model*, **https://github.com/dftd3/simple-dftd3/**.
51 H. J. Monkhorst and J. D. Pack, *Phys. Rev. B: Solid State*, 1976, **13**, 5188–5192.
52 A. Shrestha, X. Gao, J. C. Hicks and C. Paolucci, *Chem. Mater.*, 2021, **33**, 4606–4620.
53 R. J. Fries and C. P. Kempter, *Anal. Chem.*, 1960, **32**, 1898.
54 S. P. Ong, W. D. Richards, A. Jain, G. Hautier, M. Kocher, S. Cholia, D. Gunter, V. L. Chevrier, K. A. Persson and G. Ceder, *Comput. Mater. Sci.*, 2013, **68**, 314–319.
55 W. Sun and G. Ceder, *Surf. Sci.*, 2013, **617**, 53–59.
56 R. F. Ribeiro, A. V. Marenich, C. J. Cramer and D. G. Truhlar, *J. Phys. Chem. B*, 2011, **115**, 14556–14562.
57 A. Hjorth Larsen, J. Jørgen Mortensen, J. Blomqvist, I. E. Castelli, R. Christensen, M. Dułak, J. Friis, M. N. Groves, B. Hammer, C. Hargus, E. D. Hermes, P. C. Jennings, P. Bjerre Jensen, J. Kermode, J. R. Kitchin, E. Leonhard Kolsbjerg, J. Kubal, K. Kaasbjerg, S. Lysgaard, J. Bergmann Maronsson, T. Maxson, T. Olsen, L. Pastewka, A. Peterson, C. Rostgaard, J. Schiøtz, O. Schütt, M. Strange, K. S. Thygesen, T. Vegge, L. Vilhelmsen, M. Walter, Z. Zeng and K. W. Jacobsen, *J. Phys.: Condens.Matter*, 2017, **29**, 273002.
58 G. Henkelman, B. P. Uberuaga and H. Jónsson, *J. Chem. Phys.*, 2000, **113**, 9901–9904.
59 G. Henkelman and H. Jónsson, *J. Chem. Phys.*, 1999, **111**, 7010–7022.
60 K. Mathew, V. Kolluru, S. Mula, S. N. Steinmann and R. G. Hennig, *J. Chem. Phys.*, 2019, **151**, 234101.
61 K. Mathew, R. Sundararaman, K. Letchworth-Weaver, T. A. Arias and R. G. Hennig, *J. Chem. Phys.*, 2014, **140**, 084106.
62 K. Mathew, R. G. Hennig, J. Bértoli, *VASPsol: VASPsol Solvation Module, V1.0,10.5281*, DOI: **10.5281/zenodo.2555053**.
63 W. Tang, E. Sanville and G. Henkelman, *J. Phys.: Condens.Matter*, 2009, **21**, 084204.
64 M. Yu and D. R. Trinkle, *J. Chem. Phys.*, 2011, **134**, 064111.
65 G. Henkelman, A. Arnaldsson and H. Jónsson, *Comput. Mater. Sci.*, 2006, **36**, 354–360.
66 K. Reuter and M. Scheffler, *Phys. Rev. B: Condens. Matter Mater. Phys.*, 2001, **65**, 035406.
67 *CRC Handbook of Chemistry and Physics*, ed. D. R. Lide, CRC Press, Florida, 85th edn, 2004, pp. 6–8.
68 J. K. Nørskov, J. Rossmeisl, A. Logadottir, L. Lindqvist, J. R. Kitchin, T. Bligaard and H. Jónsson, *J. Phys. Chem. B*, 2004, **108**, 17886–17892.
69 B. M. Wyvratt, J. R. Gaudet and L. T. Thompson, *J. Catal.*, 2015, **330**, 280–287.
70 S. R. J. Likith, C. A. Farberow, S. Manna, A. Abdulslam, V. Stevanović, D. A. Ruddy, J. A. Schaidle, D. J. Robichaud and C. V. Ciobanu, *J. Phys. Chem. C*, 2018, **122**, 1223–1233.
71 R. A. Mir, P. Sharma and O. P. Pandey, *Sci. Rep.*, 2017, **7**, 3518.

72 Y. Chen, H. Zhang, J. Zhang, J. Ma, H. Ye, G. Qian, Y. Ye and S. Zhong, *Mater. Sci. Appl.*, 2011, **2**, 1313.
73 N. S. Alhajri, D. H. Anjum and K. Takanabe, *J. Mater. Chem. A*, 2014, **2**, 10548–10556.
74 Z. Luo, R. Miao, T. D. Huan, I. M. Mosa, A. S. Poyraz, W. Zhong, J. E. Cloud, D. A. Kriz, S. Thanneeru, J. He, Y. Zhang, R. Ramprasad and S. L. Suib, *Adv. Energy Mater.*, 2016, **6**, 1600528.
75 C. Jian, Q. Cai, W. Hong, J. Li and W. Liu, *Small*, 2018, **14**, 1703798.
76 K. A. Goulas, A. V. Mironenko, G. R. Jenness, T. Mazal and D. G. Vlachos, *Nat. Catal.*, 2019, **2**, 269–276.
77 A. V. Mironenko and D. G. Vlachos, *J. Am. Chem. Soc.*, 2016, **138**, 8104–8113.

Electronic Supplementary Material (ESI) for Journal of Materials Chemistry A.

Supporting Information

Implication of Surface Oxidation of Nanoscale Molybdenum Carbide on Electrocatalytic Activity

Siying Yu, Ankit Kumar Gautam, Di Gao, Andrew N. Kuhn, Haozhen He, Alexander V. Mironenko,* Hong Yang*

Department of Chemical and Biomolecular Engineering, University of Illinois Urbana-Champaign, 600 S. Mathews Ave., Urbana, IL, 61801, USA

* Corresponding authors: hy66@illinois.edu (HY); alexmir@illinois.edu (AM)

Computational Notes

Note S1. Computational details

Bulk cell optimization

Bulk unit cell optimization was carried out with the bulk unit cell of β-Mo_2C ($P6_3/mmc$)[1] and optimized in VASP with the ISIF of 3 to ensure relaxation of cell dimension and angle. The electronic self-consistent field loop was executed until energy values changed by less than 10^{-6} eV and forces were less than 0.02 eV/Å.

Optimal k-point mesh in slab calculations

The optimal k-space mesh was determined using the electronic binding energy of a single oxygen atom on a clean β-Mo_2C(011) surface, defined as

$$BE_O = E_{O^*} - E_{clean} - \frac{1}{2}E_{O_2} \quad \text{(S1)}$$

where E_{O^*} is the electronic energy of the slab with a single oxygen attached to an exposed carbon atom, E_{clean} is the energy of a bare slab, and E_{O_2} is the energy of an oxygen molecule. Calculations were carried out using the PBE exchange-correlation functional. Binding energy deviations were performed for each grid against the most dense $5 \times 6 \times 1$ k-point grid, along with average CPU times per one self-consistent field (SCF) iteration (diagonalization).

Comparing the calculated values in **Table S6,** the $4 \times 5 \times 1$ grid was selected for surface calculations, because it showed errors of less than 10 meV at 2/3 of the computational cost. A more affordable $2 \times 2 \times 1$ grid was used for computationally intensive NEB and HSE06 calculations.

Dipole corrections in the z-direction

We evaluated the effect of including dipole corrections in the z-direction using the binding energy of a single oxygen atom, as described above. The inclusion of dipole corrections

only changed the energy by 3 meV (see **Table S7)**. Consequently, all surface calculations do not employ dipole corrections.

Other non-default VASP settings

We made use of ISPIN = 2 (spin polarized), ISMEAR = 0, SIGMA = 0.05 eV, IVDW = 11 for DFTD3, LREAL = Auto, and ENCUT = 450 eV. During geometry optimizations, structures were initially optimized at the Γ point, the SCF termination energy criterion of 10^{-4} eV, and until forces are less than 0.1 eV/Å. These structures served as an initial guess for calculations using a $4 \times 5 \times 1$ *k*-point grid, SCF loop terminating at the 10^{-6} eV energy difference, and forces less than 0.05 eV. This two-level optimization offer the opportunity for a significant speedup in obtaining optimized geometries quickly.

NEB settings

NEB calculations employed the climbing image method[2, 3] with eight images excluding the endpoints. The transition state geometry was further corrected with the dimer method using default dimer settings and EDIFF = 1e-6 eV, EDIFFG = -0.05 eV/ Å. Vibrational frequencies were computed for the transition state to verify the presence of a single imaginary mode.

Bader charge calibration

Bader charges were computed as single point calculations at the optimized geometry with the PREC = Accurate setting in the VASP input file. Software output values were then converted to net atomic charges by subtracting them from 6 (the core charge) for Mo atoms. Oxidation states of +0, +2, and +6 were ascribed to the Bader net atomic charges obtained for bulk Mo, bulk Mo_2C, and bulk MoO_3, respectively. We observed a near-linear correlation between oxidation states and Bader atomic charges and established the following relationship (**Figure S1**):

$$\text{Oxidation state} = 2.51 \times \text{BaderNetAtomicCharge} + 0.13 \quad (S2)$$

Gibbs free energy and solvation correction

We computed the vibrational frequencies of the adsorbates (every species on the surface except slab Mo and C) and treated them using the harmonic oscillator approximation. Frequencies under 100 cm^{-1} were shifted up to 100 cm^{-1}. We approximated Gibbs free energy G as Helmholtz free energy F by neglecting the PV term, according to **Equation S3**. A temperature of 298.15 K was used in all calculations.

$$G = F = E_{elec} + E_{ZPE} + \int_0^T C_{V,vib}\ dT - TS_{harmonic} \quad (S3)$$

We used VASPsol[4-6] to describe the solvation environment implicitly with the PBE functional and added the energy correction onto the HSE06 electronic energies:

$$G_{HSE06} = E_{elec,HSE06} + (G_{PBE} - E_{PBE}) + (E_{PBE,VASPSOL} - E_{PBE}) \quad (S4)$$

The corrections terms in **Equation S4** allow us to use solvation stabilization and the vibrational frequencies with a much faster PBE exchange-correlation functional, since both vibration and solvation effects have much less influence on relative energies than that with the electronic energy and largely cancel out in energy differences (**Table S1**).

Note S2. Gibbs free energy of formation of chemisorbed species

Binding energy of adsorbates at low coverage

We computed the adsorption energies of O*/H*/OH*/H_2O* on the clean surface according to **Equations S5-S8**, respectively, as shown below,

$$Mo_xC_y + H_2O\ (liq) \rightarrow Mo_xC_y|O^* + 2(H^+ + e^-) \quad (S5)$$

$$Mo_xC_y + H_2O\ (liq) \rightarrow Mo_xC_y|OH^* + H^+ + e^- \quad (S6)$$

$$Mo_xC_y + H^+ + e^- \ \rightarrow Mo_xC_y|H^* \quad (S7)$$

$$Mo_xC_y + H_2O(liq) \ \rightarrow Mo_xC_y|H_2O^* \quad (S8)$$

In **Table S8,** we report the binding energies of chemisorbed species at the lowest possible coverage at U_{RHE} = 0 V for the (3×1) β-$Mo_2C(011)$ supercell. All energies are in eV.

Note S3. C*-to-O* substitutiton reaction

The C* to O* substitution reaction, also referred to as substitutive oxidation, was assumed to proceed through the following steps on a partially oxidized surface containing *n* O* atoms:

1. "Additive" oxidation of the surface

$$Mo_xC_y\left|O_n^*\right. + H_2O(liq) \rightarrow Mo_xC_y\left|O_{n+1}^*\right. + 2(H^+ + e^-) \quad (S9)$$

2. CO desorption to form carbon vacancy

$$Mo_xC_y\left|O_{n+1}^*\right. \rightarrow Mo_xC_{y-1}\left|O_n^*\right. + CO(g) \quad (S10)$$

3. "Additive" oxidation on the carbon vacancy

$$Mo_xC_{y-1}\left|O_n^*\right. + H_2O(liq) \rightarrow Mo_xC_{y-1}\left|O_{n+1}^*\right. + 2(H^+ + e^-) \quad (S11)$$

The net effect amounts to C* replacement with O* and the production of one CO molecule and 4 $(H^+ + e^-)$ pairs in the process. Due to the strong stabilization associated with proton-electron pair generation, substitutive oxidation is exergonic at all positive potentials (**Table S9** and **Figure S15**).

Note S4. CO and CO_2 desorption barriers

To evaluate the kinetics of this thermodynamically favorable substitution process, we assumed vacancy reoxidation to be fast due to the high oxophilicity of Mo. Thus, vacancy formation through CO/CO_2 removal is the rate-limiting step (RLS). Since CO_2 formation is associated with nearly complete detachment of CO* in the transition state (**Table S5**) and exhibits greater barriers than for the removal of CO (**Table 4**), we used the computed barrier for CO removal as a kinetic stability metric of oxidized surfaces. The transition state structures are obtained through CI-NEB and the dimer method. All values are in eV (**Table S5**).

Note S5. Water binding energies at oxidized surfaces

We calculated water adsorption energies on pre-determined, oxidized surfaces (**Table S4**).

Note S6. Charge transfer estimation

To obtain an order-of-magnitude estimate of the amount of charge produced in various surface oxidation processes, we employed a simplified model of a catalyst. The calculation proceeds as follows:

$$\begin{aligned}\text{Total Charge} = &(\text{Charge of } 2\ e^-) \\ \times\ &(\text{Number of O}^*\text{added} + 2 \times \text{number of C substituted}) \\ &\times (\text{Estmated area of all deposited nanoparticles}) \\ &/(\text{Area of } 3 \times 1 \text{ supercell})\end{aligned} \qquad (S12)$$

where the charge generated from one O* deposition is 2 e^-.

To get the ratio of areas (*i.e.*, the number of supercells in the material), we first determined the amount of Mo_2C formed from the amount of a precursor, assuming total conversion of Mo to carbide during carburization:

$$\text{Moles of } Mo_2C \text{ formed} = \frac{7}{2}\text{Moles of } ((NH_4)_6Mo_7O_{24} \cdot 4H_2O) \qquad (S13)$$

To determine the amount of Mo_2C on the electrode, we took into account the Mo_2C:carbon black mass ratio, the weight of a β-Mo_2C sample (3 mg), and the dilution factor during ink-drop cast of the electrode to get 9.61 μg of catalyst on a single electrode. Using 8.9 g/cm^3 density for β-Mo_2C and assuming perfectly spherical uniform 5 nm nanoparticles, we get 1.65e+13 nanoparticles on the electrode exposing a total of 1.30e-3 m^2 area. Since each computational supercell exposes 6.35e-19 m^2, we get a total 2.04e+15 unit cells. Applying **Equation S12,** we get

$$\text{Charge per O* addition} = 2 \times 1.6 \times 10^{-19} \times 2.04 \times 10^{15} \text{ mC} \qquad (S14)$$

$$\text{Charge per O* addition} = 0.65 \text{ mC}$$

Using this value, we found that the $(Mo\text{-}O)_1(C\text{-}O)_6$ to $(Mo\text{-}O)_3(C\text{-}O)_6$ change produces 1.31 mC since it involves deposition of 2 O*. On the other hand, $(Mo\text{-}O)_3(C\text{-}O)_6$ to $(Mo\text{-}O)_4(C\text{-}O)_6$ gives rise to 0.65 mC. Furthermore, achieving the surface $(Mo\text{-}O)_{12}(C\text{-}O)_0$ from $(Mo\text{-}O)_3(C\text{-}O)_6$, involves deposition of 11 O* (6 of which are removed in the CO desorption), generating a charge of 7.18 mC.

Note S7. Current estimation

We carried out a similar calculation of current densities during slow and fast substitutive oxidation using the obtained energy barrier values.

$$rate = \frac{k_B T}{h} \exp\left(\frac{-E_a}{k_B T}\right) \left[\frac{1}{\text{sec}\cdot\text{site}}\right] \qquad (S15)$$

In this analysis, we counted the total number of exposed C sites to be 1.22e+16 and obtained the estimates of current for oxidation because of CO desorption (**Table S3**).

Figures

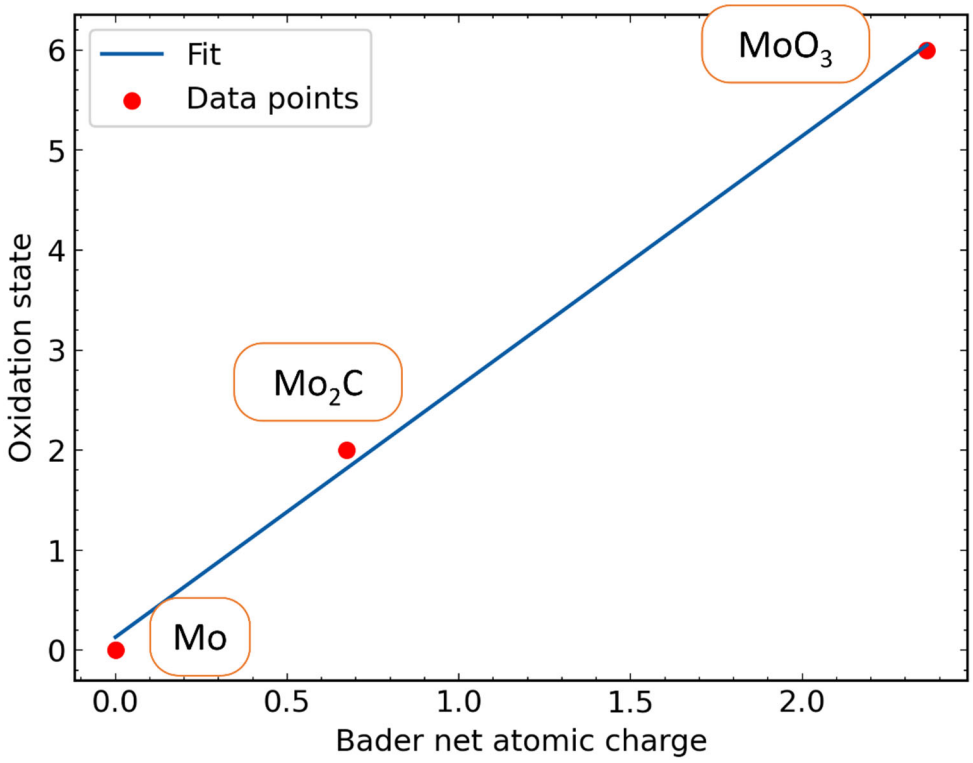

Figure S1. Calibration curve for Bader charges and oxidation states.

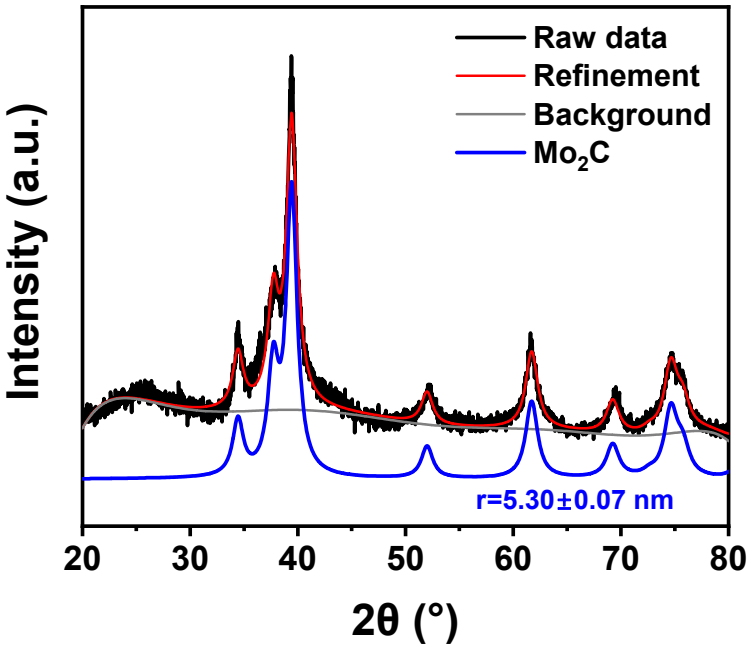

Figure S2. Volume-weighted mean crystallite size (r) analysis based on the full-profile Rietveld refinement, using the TOPAS software. The calculation is based on Scherrer equation.

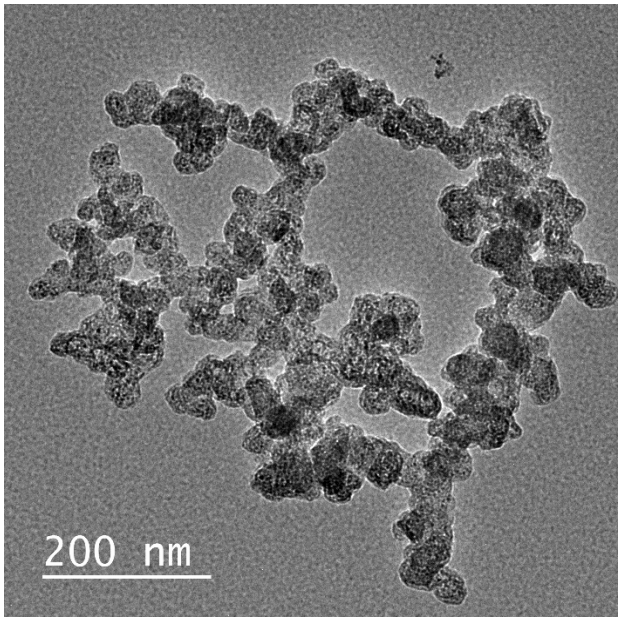

Figure S3. TEM micrograph of as-made β-Mo_2C sample.

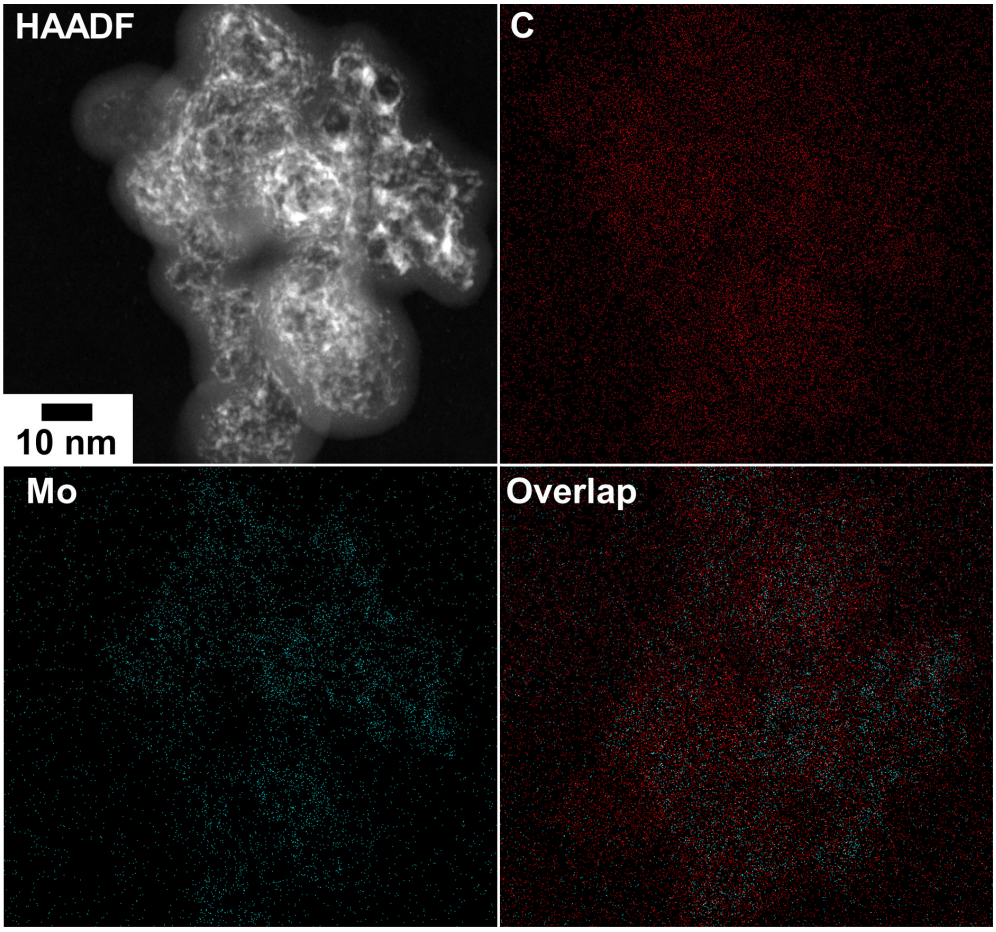

Figure S4. STEM-EDS micrographs of as-prepared β-Mo_2C nanoparticles: (red: carbon; blue: Mo).

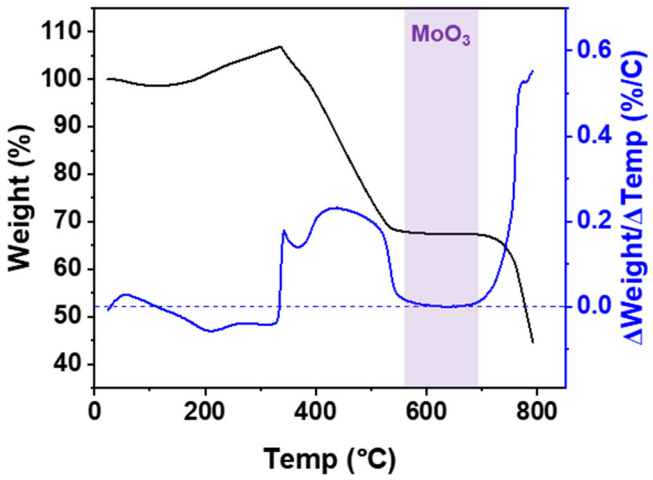

Figure S5. Thermogravimetric analysis of freshly prepared β-Mo2C sample. The purple region represents the stable MoO_3 phase.[7-9]

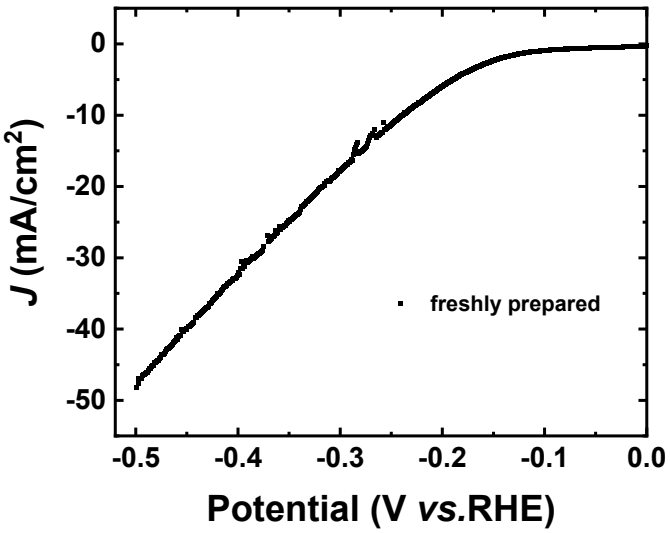

Figure S6. HER polarization curve of as-prepared β-Mo_2C catalyst without the electrochemical oxidation treatment.

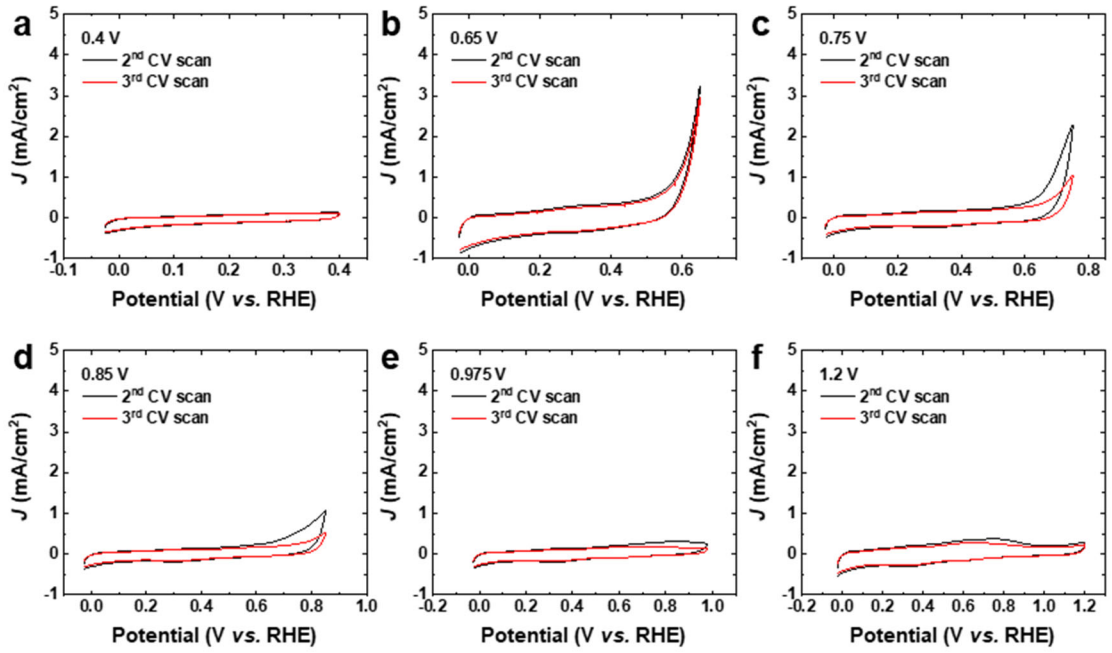

Figure S7. CV curves for the second and third cycles of the electrochemical oxidation treatment under different potential windows.

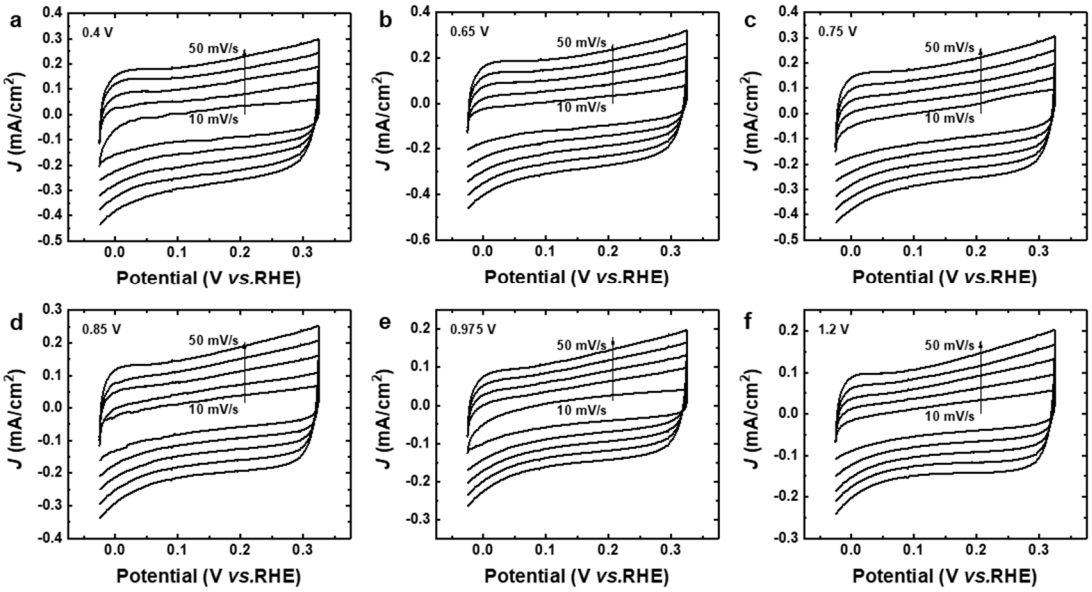

Figure S8. Measurement of double-layer capacitance. Cyclic voltammetry curves of oxidized β-Mo_2C-*x* catalysts scanned from 10 to 50 mV/s, where *x* is (a) 0.4, (b) 0.65, (c) 0.75, (d) 0.85, (e) 0.975, and (f) 1.2.

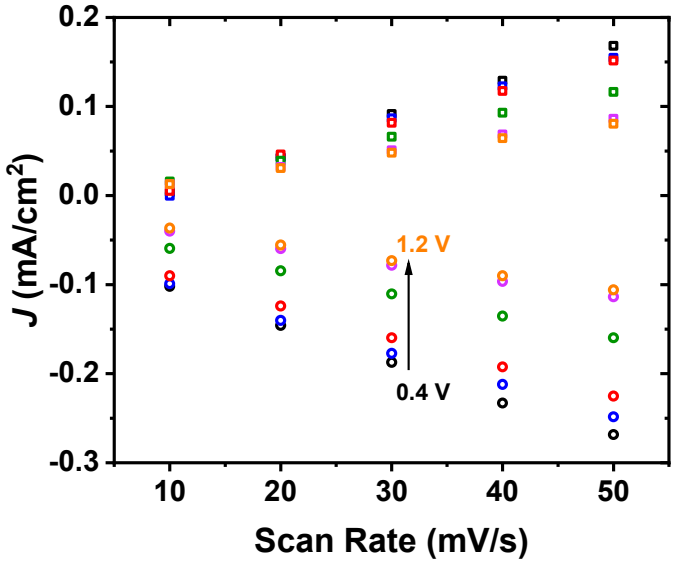

Figure S9. Capacitive current densities recorded at 0.15 V as a function of scan rate for electrochemically oxidized β-Mo_2C-*x* catalysts (square: positive scans, circle: negative scans).

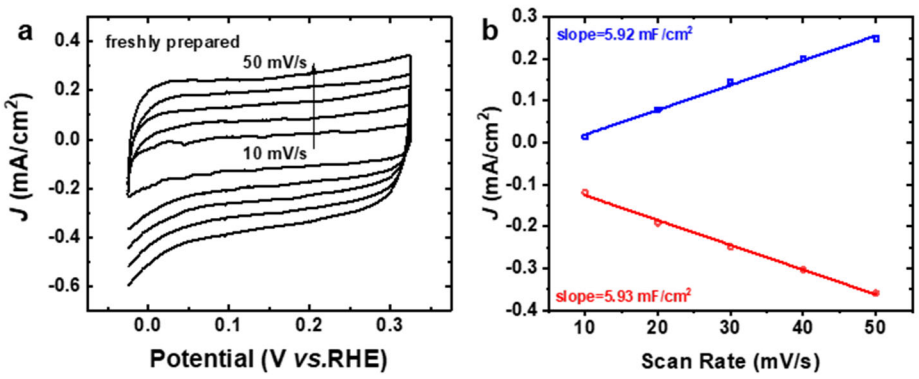

Figure S10. (a) CV curves and (b) capacitive current densities as a function of scan rate of as-prepared β-Mo_2C catalysts. The CV scans were at various rates between 10 and 50 mV/s with an increment of 10 mV/s. The capacitive current densities were measured at 0.15 V.

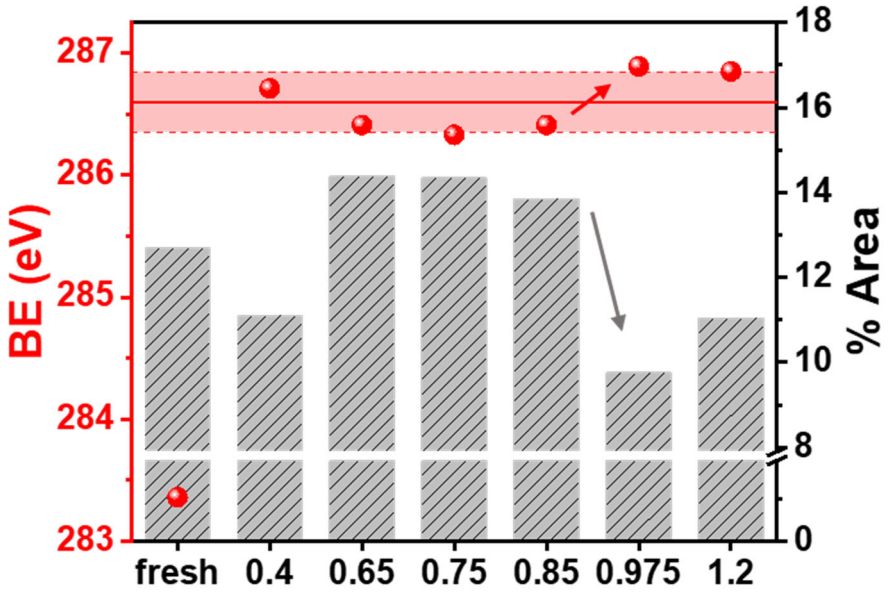

Figure S11. XPS analysis showing the position of the broad peaks centered around 286.6 eV in the C 1s region of β-Mo_2C-*x* (left axis) and the corresponding percentage of peak area (right axis). The pink strip represents the averaged peak positions, in 1σ standard deviation, for β-Mo_2C-*x* (*x*=0.4, 0.65, 0.75, 0.85, 0.975, and 1.2). The carbidic C-Mo peak for freshly prepared Mo_2C is included as the reference.

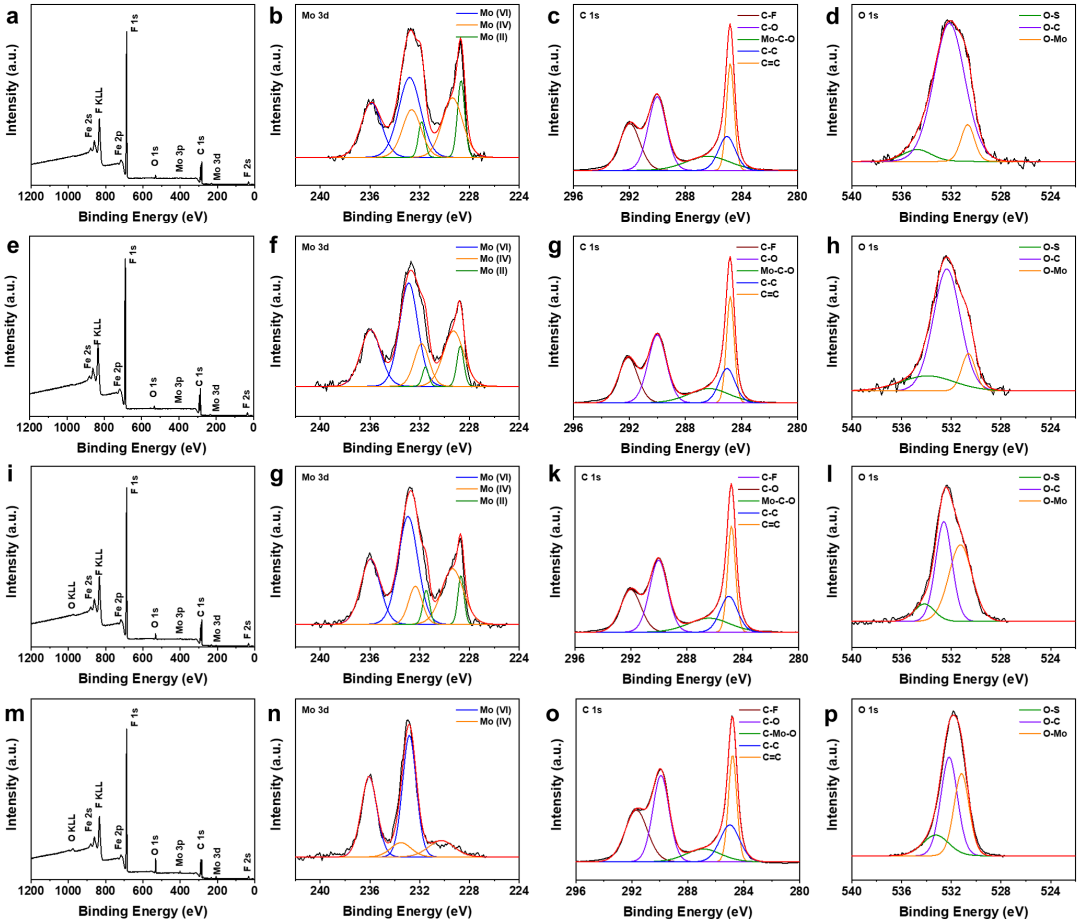

Figure S12. XPS of survey scan, Mo 3d, C 1s, and O 1s for β-Mo_2C-*x*, where *x* is (a-d) 0.65, (e-h) 0.75, (i-l) 0.85, and (m-p) 0.975.

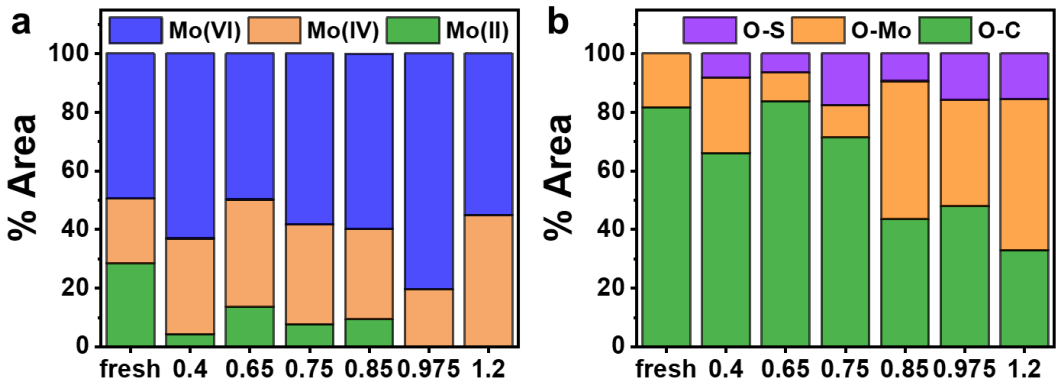

Figure S13. Analysis of the XPS peak areas for (a) Mo and (b) O for samples treated under different potentials.

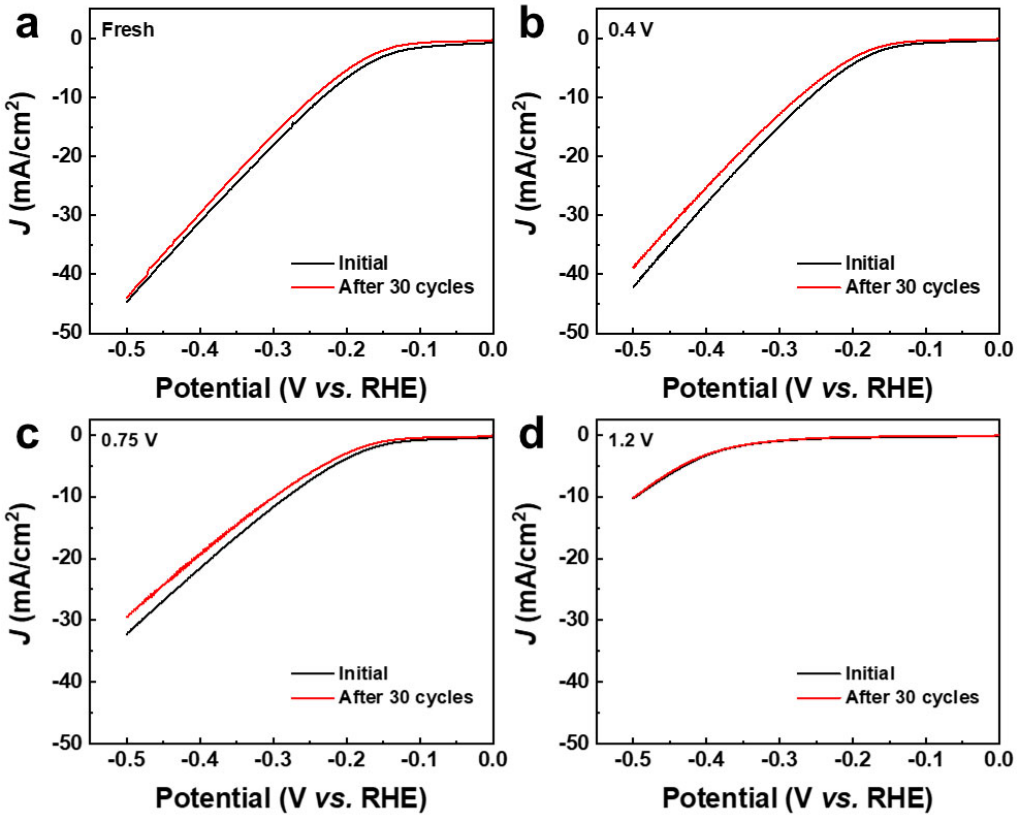

Figure S14. Polarization curves of freshly prepared and oxidized β-Mo_2C-*x* (*x*=0.4, 0.75, and 1.2) electrocatalysts for HER before and after 30 CV cycles in the range of 0~-0.5 V (*vs.* RHE).

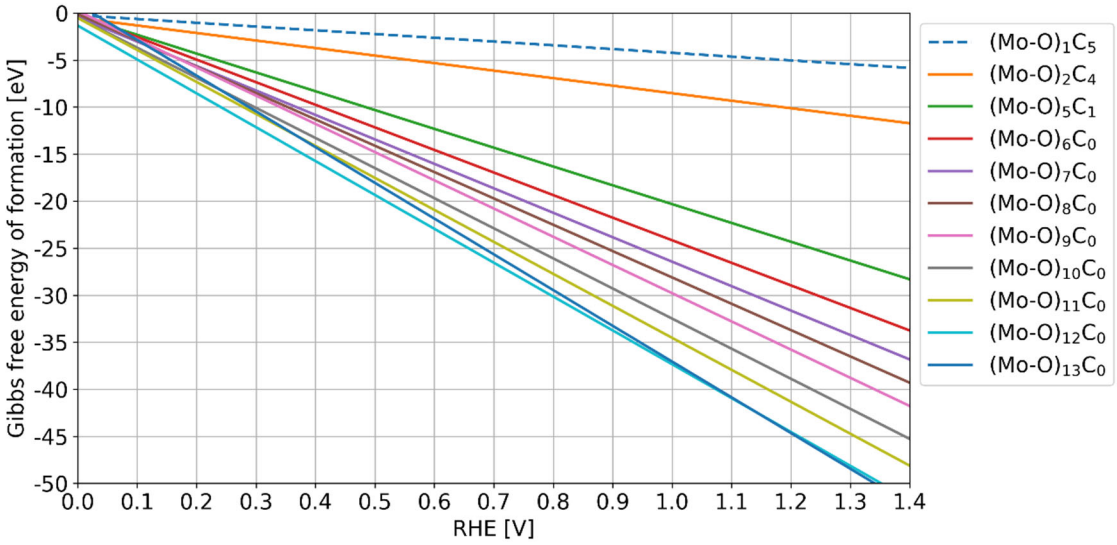

Figure S15: Gibbs free energy for the formation of C*-to-O* substituted surfaces.

Tables

Table S1. Values of Gibbs free energy for the molecules studied in this work*

Molecule	PBE	HSE06
H_2	-6.806	-7.869
H_2O	-14.218	-17.468
CO	-15.165	-18.600
CO_2	-23.205	-28.634

*: All values are in eV.

Table S2. Results of XPS analyses

β-Mo_2C (as-prepared)					
Name	Position (eV)	ΔBE (eV)	% Area	Area ratio	FWHM
O-C	531.98	/	81.69	/	3.07
O-Mo	530.61	/	18.31	/	1.17
C-O	286.76	/	19.91	/	5.4
C-C	284.98	/	38.79	/	1.97
C=C	284.8	/	28.6	/	0.77
C-Mo	283.36	/	12.7	/	1.27
Mo (VI) $3d_{3/2}$	235.89	2.84	19.33	0.64198	1.97
Mo (VI) $3d_{5/2}$	233.05	/	30.11	/	1.81
Mo (IV) $3d_{3/2}$	232.37	2.53	8.41	0.61477	1.23
Mo (IV) $3d_{5/2}$	229.84	/	13.68	/	1.56
Mo (II) $3d_{3/2}$	232.7	3.91	12.49	0.7816	1.4
Mo (II) $3d_{5/2}$	228.79	/	15.98	/	0.99
β-Mo_2C-0.4					
Name	Position (eV)	ΔBE (eV)	% Area	Area ratio	FWHM
O-S	534.2115	/	8.15	/	1.69747
O-C	532.3142	/	66.07	/	1.82613
O-Mo	530.9864	/	25.78	/	1.71839
C-F	291.8787	/	20.65	/	1.67585
C-O	290.0209	/	30.18	/	1.58875
Mo-C-O	286.7055	/	11.11	/	2.98918
C-C	284.9736	/	17.88	/	1.53751
C=C	284.7822	/	20.18	/	0.66305
Mo (VI) $3d_{3/2}$	235.9543	3.0678	22.73	0.5636	1.69433
Mo (VI) $3d_{5/2}$	232.8865	/	40.33	/	1.8793
Mo (IV) $3d_{3/2}$	232.4047	3.1317	11.51	0.54524	1.89608
Mo (II) $3d_{3/2}$	230.813	2.0952	1.51	0.53737	0.5779
Mo (IV) $3d_{5/2}$	229.273	/	21.11	/	1.91918

Mo (II) $3d_{5/2}$	228.7178	/	2.81	/	0.578
β-Mo_2C-0.65					
Name	Position (eV)	ΔBE (eV)	% Area	Area ratio	FWHM
O-S	534.7407	/	6.47	/	2.65846
O-C	532.1506	/	83.82	/	2.95505
O-Mo	530.6793	/	9.71	/	1.28373
C-F	291.9772	/	22.06	/	1.70079
C-O	290.0222	/	31	/	1.51986
Mo-C-O	286.4065	/	14.38	/	3.65095
C-C	285.0408	/	13.38	/	1.42234
C=C	284.8	/	19.17	/	0.64689
Mo (VI) $3d_{3/2}$	235.89	3.0803	19.32	0.63427	1.93371
Mo (VI) $3d_{5/2}$	232.8097	/	30.46	/	2.08344
Mo (IV) $3d_{3/2}$	232.6444	3.2793	15.47	0.73144	1.76998
Mo (II) $3d_{3/2}$	231.8482	3.1783	3.97	0.41225	0.60493
Mo (IV) $3d_{5/2}$	229.3651	/	21.15	/	1.93922
Mo (II) $3d_{5/2}$	228.6699	/	9.63	/	0.67946
β-Mo_2C-0.75					
Name	Position (eV)	ΔBE (eV)	% Area	Area ratio	FWHM
O-S	533.9025	/	117.52	/	5.10628
O-C	532.3564	/	71.37	/	2.57159
O-Mo	530.619	/	11.11	/	1.30416
C-F	292.0926	/	21.21	/	1.60123
C-O	290.017	/	30.72	/	1.55048
Mo-C-O	286.3333	/	14.35	/	3.43975
C-C	285.0323	/	13.62	/	1.35511
C=C	284.8	/	20.1	/	0.64813
Mo (VI) $3d_{3/2}$	235.9501	3.064	21.77	0.59627	1.90902
Mo (VI) $3d_{5/2}$	232.8861	/	36.51	/	1.74481
Mo (IV) $3d_{3/2}$	231.846	2.5652	12.3	0.56656	1.4238

Mo (II) $3d_{3/2}$	231.5364	2.8037	2.33	0.43309	0.58767
Mo (IV) $3d_{5/2}$	229.2808	/	21.71	/	1.92779
Mo (II) $3d_{5/2}$	228.7327	/	5.38	/	0.65256

β-Mo_2C-0.85

Name	Position (eV)	ΔBE (eV)	% Area	Area ratio	FWHM
O-S	534.165	/	9.4	/	1.93386
O-C	532.5974	/	43.49	/	1.56649
O-Mo	531.2625	/	47.11	/	2.21014
C-F	292.0062	/	20.48	/	1.70086
C-O	290.0153	/	30.79	/	1.51909
Mo-C-O	286.4082	/	13.85	/	3.50515
C-C	284.9947	/	14.91	/	1.47076
C=C	284.8	/	19.97	/	0.66622
Mo (VI) $3d_{3/2}$	235.9605	3.021	22.32	0.59472	1.8292
Mo (VI) $3d_{5/2}$	232.9395	/	37.53	/	1.86242
Mo (IV) $3d_{3/2}$	232.351	2.9862	9.13	0.42132	1.28478
Mo (II) $3d_{3/2}$	231.4763	2.795	4.08	0.77567	0.63659
Mo (IV) $3d_{5/2}$	229.3648	/	21.67	/	2.08254
Mo (II) $3d_{5/2}$	228.6813	/	5.26	/	0.57298

β-Mo_2C-0.975

Name	Position (eV)	ΔBE (eV)	% Area	Area ratio	FWHM
O-S	533.248	/	15.82	/	2.48381
O-C	532.1743	/	47.89	/	1.57908
O-Mo	531.1761	/	36.29	/	1.43687
C-F	291.6847	/	25.02	/	1.89404
C-O	289.9226	/	30.49	/	1.38207
Mo-C-O	286.8932	/	9.76	/	2.98105
C-C	284.9986	/	15.57	/	1.65449
C=C	284.8	/	19.16	/	0.70041
Mo (VI) $3d_{3/2}$	236.0738	3.2426	34.47	0.75065	1.48774

Mo (IV) $3d_{3/2}$	233.5117	3.2462	7.97	0.68471	1.92654
Mo (VI) $3d_{5/2}$	232.8312	/	45.92	/	1.30572
Mo (IV) $3d_{5/2}$	230.2655	/	11.64	/	2.4563

β-Mo_2C-1.2

Name	Position (eV)	ΔBE (eV)	% Area	Area ratio	FWHM
O-S	533.0158	/	15.56	/	3.42747
O-C	532.1774	/	32.97	/	1.99856
O-Mo	531.5116	/	51.48	/	1.83032
C-F	291.5644	/	24.37	/	2.00869
C-O	289.9701	/	27.67	/	1.35202
Mo-C-O	286.8508	/	11.05	/	3.13211
C-C	284.9174	/	18.29	/	1.60281
C=C	284.8	/	18.62	/	0.72021
Mo (VI) $3d_{3/2}$	236.0539	3.1551	21.69	0.64999	1.22954
Mo (IV) $3d_{3/2}$	233.2753	4.4541	18.62	0.70745	6.67
Mo (VI) $3d_{5/2}$	232.8988	/	33.37	/	1.20159
Mo (IV) $3d_{5/2}$	228.8212	/	26.32	/	6.67388

Table S3. Computationally obtained parameters

Potential (V)	Barrier for CO desorption (eV)	Current density (mA/cm^2)
0.28	0.71	1.24e+2
0.51	0.07	8.15e+12

Table S4. Computational results of water adsorption energy on oxidized surfaces of Mo_2C

Starting Surface	ΔG Binding energy (eV)
$(Mo\text{-}O)_0(C\text{-}O)_0$	-1.06
$(Mo\text{-}O)_0(C\text{-}O)_6$	-0.30
$(Mo\text{-}O)_1(C\text{-}O)_6$	-0.13
$(Mo\text{-}O)_2(C\text{-}O)_6$	-0.1
$(Mo\text{-}O)_3(C\text{-}O)_6$	0.19

Table S5. Energy barriers for CO and CO_2 desorptions with transition states at HSE refined single point energies. Numbers in parentheses are barriers in eV obtained using PBE functional

Surface	CO	CO_2
$(Mo\text{-}O)_0(C\text{-}O)_1$	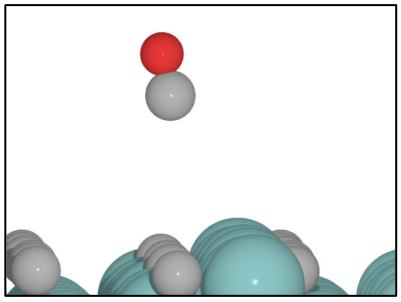 1.39 (1.72) No TS found	-
$(Mo\text{-}O)_0(C\text{-}O)_6$	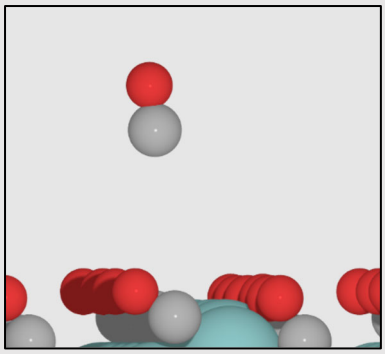 1.79 (1.98) No TS found	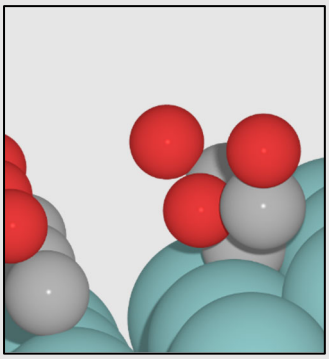 2.58 (2.44)
$(Mo\text{-}O)_1(C\text{-}O)_6$	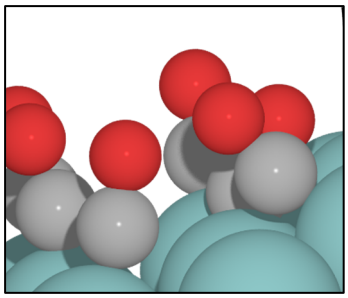 1.61 (1.18)	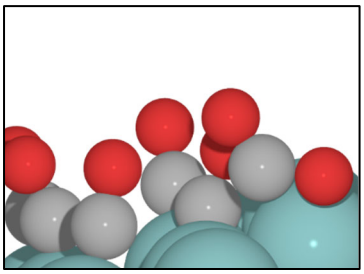 2.75 (2.34)
$(Mo\text{-}O)_3(C\text{-}O)_6$	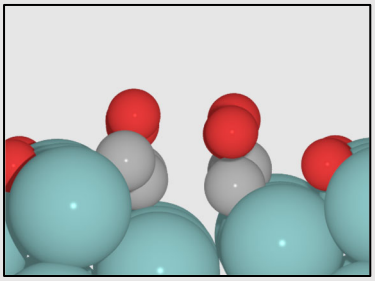 Type 1: 0.73 (0.84)	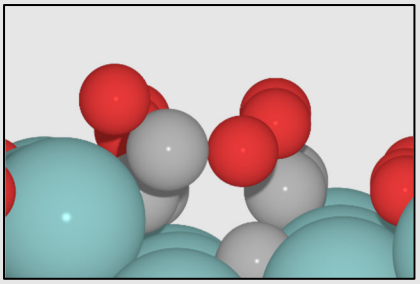 1.05 (1.11)

	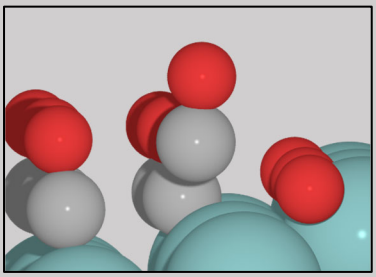 Type 2: 0.71 (0.83)	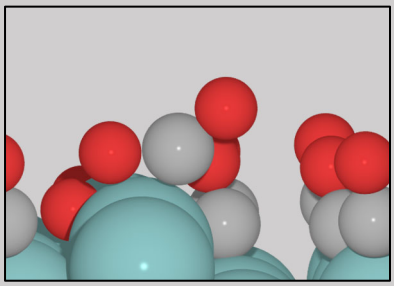 1.37 (1.53)
$(Mo\text{-}O)_4(C\text{-}O)_6$	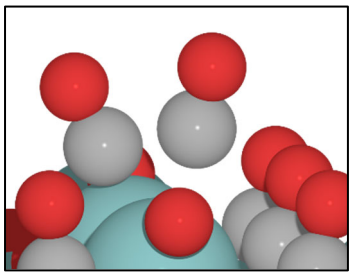 0 (0.07)	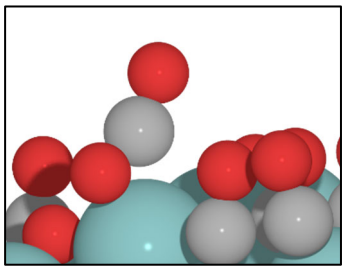 0.07 (0.07)

Cyan, Grey and Red balls represent Mo, C and O atoms respectively.

We also simulated CO desorption on a surface formed after substitution of three CO* molecules with three O* atoms, for which the PBE barrier was found to be 0.59 (0.47) eV.

Table S6. Convergence criteria for *k* point grid for surface calculations

k-point grid	ΔBE_O (eV) (against 5×6×1)	Time for 1 iteration within SCF loop (s)
1×1×1	0.485	0.34
2×2×1	-0.029	0.37
3×3×1	-0.017	1.23
4×5×1	0.007	1.86
5×6×1	0	2.76

Table S7. Influence of dipole corrections on oxygen binding energy*

	E_{clean}	E_{O^*}	$\frac{1}{2}E_{O_2}$	BE_O
No dipole	-405.546	-413.846	-4.924	-3.375
With dipole correction	-405.541	-413.843	-4.924	-3.378

*: All values are in eV.

Table S8. Binding sites for individual H_2O derived species with their energies in eV

Species	Mo	C site
O*	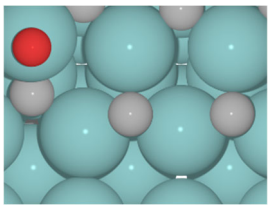 ΔG = -0.26	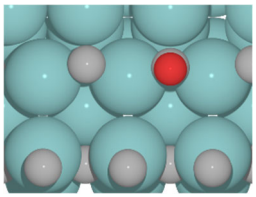 ΔG = -0.47
OH*	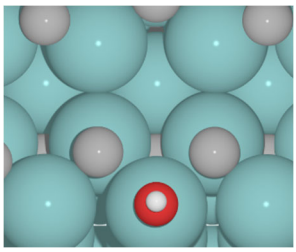 ΔG = -0.64	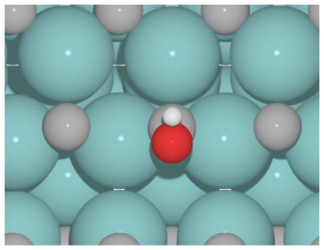 ΔG = -0.33
H*	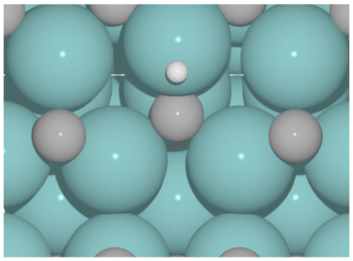 ΔG = -0.16	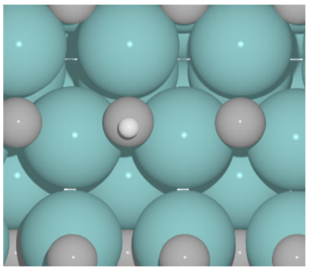 ΔG = -1.12
H_2O*	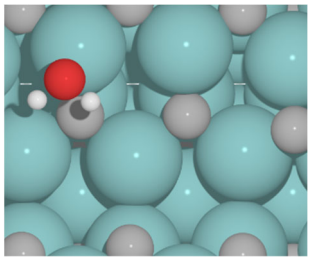 ΔG = -1.06	H_2O moved to Mo or desorbs from the surface

Table S9. Gibbs free energy change for replacement of single C* to O* at two coverages

Surface prior to substitution	ΔG at U_{RHE} = 0 V (eV)	ΔG at U_{RHE} = 1.2 V (eV)
$(Mo\text{-}O)_0(C\text{-}O)_1$	-0.22	-5.02
$(Mo\text{-}O)_0(C\text{-}O)_6$	-1.02	-5.82

References

1. A. Shrestha, X. Gao, J. C. Hicks and C. Paolucci, *Chem. Mater.*, 2021, **33**, 4606-4620.
2. G. Henkelman, B. P. Uberuaga and H. Jónsson, *J. Chem. Phys.*, 2000, **113**, 9901-9904.
3. G. Henkelman and H. Jónsson, 2000, **113**, 9978-9985.
4. K. Mathew, V. Kolluru, S. Mula, S. N. Steinmann and R. G. Hennig, *J. Chem. Phys.*, 2019, **151**, 234101.
5. K. Mathew, R. Sundararaman, K. Letchworth-Weaver, T. A. Arias and R. G. Hennig, *J. Chem. Phys.*, 2014, **140**, 084106.
6. K. Mathew, Rhennig and J. Bértoli, VASPsol: VASPsol Solvation Module V1.0, https://doi.org/10.5281/zenodo.2555053.
7. R. A. Mir, P. Sharma and O. P. Pandey, *Sci. Rep.*, 2017, **7**, 3518.
8. Y. Chen, H. Zhang, J. Zhang, J. Ma, H. Ye, G. Qian, Y. Ye and S. Zhong, *Mater. Sci. Appl.*, 2011, **2**, 1313.
9. N. S. Alhajri, D. H. Anjum and K. Takanabe, *J. Mater. Chem. A*, 2014, **2**, 10548-10556.